

DTIC FILE COPY

2



University of Maryland, College Park  
Department of Aerospace Engineering

AD-A229 015

AFOSR-TE- 90A 1188

Final Report on AFOSR Grant No. 88-0107

NON-EQUILIBRIUM CHEMISTRY EFFECTS ON HYPERSONIC  
SEPARATED FLOWS--SHOCK-WAVE/BOUNDARY-LAYER INTERACTION

by

John D. Anderson, Jr.

Professor

Department of Aerospace Engineering

University of Maryland

College Park, Maryland 20742

DTIC  
ELECTE  
NOV 16 1990  
S B D

September 27, 1990

DISTRIBUTION STATEMENT A

Approved for public release;  
Distribution Unlimited

UNCLASSIFIED

SECURITY CLASSIFICATION OF THIS PAGE

## REPORT DOCUMENTATION PAGE

1a. REPORT SECURITY CLASSIFICATION Unclassified			1b. RESTRICTIVE MARKINGS		
2a. SECURITY CLASSIFICATION AUTHORITY N/A			3. DISTRIBUTION/AVAILABILITY OF REPORT Approved for public release. Distribution is unlimited.		
2b. DECLASSIFICATION/DOWNGRADING SCHEDULE N/A					
4. PERFORMING ORGANIZATION REPORT NUMBER(S)			5. MONITORING ORGANIZATION REPORT NUMBER(S)		
6a. NAME OF PERFORMING ORGANIZATION Dept. of Aerospace Engineering University of Maryland		6b. OFFICE SYMBOL (If applicable) NA	7a. NAME OF MONITORING ORGANIZATION AFOSR/NA		
6c. ADDRESS (City, State, and ZIP Code) College Park, Maryland 20742-3015			7b. ADDRESS (City, State, and ZIP Code) Building 410 Bolling AFB, Washington, D.C. 20332-6448		
8a. NAME OF FUNDING/SPONSORING ORGANIZATION AFOSR		8b. OFFICE SYMBOL (If applicable) NA	9. PROCUREMENT INSTRUMENT IDENTIFICATION NUMBER AFOSR-88-0127		
8c. ADDRESS (City, State, and ZIP Code) Building 410 Bolling AFB, Washington, D.C. 20332-6448			10. SOURCE OF FUNDING NUMBERS		
			PROGRAM ELEMENT NO. 61102	PROJECT NO. 2307	TASK NO. A1
11. TITLE (Include Security Classification) Non-Equilibrium Chemistry Effects on Separated High-Speed Flows in Air.					
12. PERSONAL AUTHOR(S) Anderson, John D., Jr.					
13a. TYPE OF REPORT Final		13b. TIME COVERED FROM 880301 TO 900228		14. DATE OF REPORT (Year, Month, Day) 900927	
15. PAGE COUNT 65					
16. SUPPLEMENTARY NOTATION					
17. COSATI CODES			18. SUBJECT TERMS (Continue on reverse if necessary and identify by block number)		
FIELD	GROUP	SUB-GROUP	Separated Flow , Shock-Wave/Boundary Layer, Non-Equilibrium, Boundary Layer interaction. (✓)		
	20.04				
19. ABSTRACT (Continue on reverse if necessary and identify by block number) This work has addressed the question: What is the effect of nonequilibrium chemical reactions on separated hypersonic flow? The model used to generate the separated flow is a hypersonic shock wave/boundary layer interaction on a flat plate in a high enthalpy flow. The flow was calculated by means of a finite-difference, time-marching solution. The results show that nonequilibrium effects can be important in the separated flow region, and that future applications should be aware of such effects.					
20. DISTRIBUTION/AVAILABILITY OF ABSTRACT <input type="checkbox"/> UNCLASSIFIED/UNLIMITED <input checked="" type="checkbox"/> SAME AS RPT. <input type="checkbox"/> DTIC USERS			21. ABSTRACT SECURITY CLASSIFICATION Unclassified		
22a. NAME OF RESPONSIBLE INDIVIDUAL Dr. Len Sakell			22b. TELEPHONE (Include Area Code) (202) 767-4935		22c. OFFICE SYMBOL AFOSR/NA

UNCLASSIFIED

Final Report on AFOSR Grant No. 88-0107

NON-EQUILIBRIUM CHEMISTRY EFFECTS ON HYPERSONIC  
SEPARATED FLOWS--SHOCK-WAVE/BOUNDARY-LAYER INTERACTION

by

John D. Anderson, Jr.  
Professor  
Department of Aerospace Engineering  
University of Maryland  
College Park, Maryland 20742

September 27, 1990

I. INTRODUCTORY COMMENTS:

Question: What is the effect of nonequilibrium chemical reactions on hypersonic separated flow? This question can be an important consideration for some aspects of the high enthalpy flows over hypersonic vehicles. However, the fundamental answer to this question has never been obtained, either experimentally or computationally. Indeed, to the author's knowledge, this problem has never been addressed in the context of a fundamental research study. Such is the purpose of the present work. In particular, computational fluid dynamics is used to calculate a hypersonic separated flow in air, first without chemical reactions, and then with nonequilibrium chemical reactions. The results are compared, and some of the fundamental physical effects caused by the chemically reacting flow are elucidated and studied.

The details of the analyses are given in Appendices A and B. In Appendix A, the nonequilibrium chemically reacting shock wave/boundary layer flow was studied from the point of view of the basic flow properties, with varying shock strength as a parameter. In Appendix B, the influence of catalytic wall surfaces was studied. The computational technique in both cases was a time-marching explicit finite-difference solution of the full two-dimensional Navier-Stokes Equations coupled with finite-rate chemical reactions. The reacting model was a five-species, five reaction model for high temperature air deemed suitable for the present investigation.

## II. RESULTS

The results are also detailed in Appendices A and B; hence no elaboration will be given here.

## III. CONCLUSIONS

The results of the present study, as embodied in Appendices A and B, clearly show that nonequilibrium chemical reactions in a hypersonic separated flow, as modeled by a shock-wave/boundary layer interaction, can have a substantial effect on the details of the flow as well as the surface heat transfer, as compared to the nonreacting case. Specifically, the reacting effects lead to increased heat transfer, as well as a restructuring of the pressure distribution and the shape of the separated flow region. This investigation is the first to study in a fundamental manner the effects of nonequilibrium chemical reactions on hypersonic separated flow. The results indicate

For	<input checked="" type="checkbox"/>
1	<input type="checkbox"/>
1	<input type="checkbox"/>
on	
on/	



Availability Codes	
Dist	Avail and/or Special
A-1	

that future applications involving such flows should keep such effects in mind, and should take them into account as necessary.

#### IV. FINAL COMMENT

This work will be reported at the AIAA 29th Aerospace Sciences Meeting in Reno, Nevada, January 1991. The substance of this work is given in Appendices A and B. Appendix A is an advance copy of AIAA Paper No. 91-0250, and Appendix B is an extended abstract which forms the basis of AIAA Paper No. 91-0245.

## Appendix A



**AIAA 91-0250**

**Shock Strength Effects on  
Separated Flows in Non-Equilibrium  
Chemically Reacting Air  
Shock Wave/Boundary Layer Interaction**

**C. A. Ballaro and J. D. Anderson, Jr.**

**University of Maryland  
College Park, MD**

**29th Aerospace Science Meeting**

**January 7-10, 1991 / Reno, Nevada**

# SHOCK STRENGTH EFFECTS ON SEPARATED FLOWS IN NON-EQUILIBRIUM CHEMICALLY REACTING AIR — SHOCK WAVE/BOUNDARY LAYER INTERACTION

by  
Charles A. Ballaro\*  
and  
John D. Anderson, Jr.†  
Department of Aerospace Engineering  
University of Maryland  
College Park, MD 20742

## Abstract

This work is part of a general study to examine the effects of nonequilibrium chemical reactions on hypersonic separated flows. In particular, the work presented is the first attempt to quantitatively predict the effects of impinging shock strength on the separation region in non-equilibrium chemically reacting air over a flat plate. Of special interest is the local heat transfer rate to the plate at the reattachment point. The effects of chemical non-equilibrium on the flow field are assessed by making direct comparisons to the results calculated assuming a calorically perfect flow. Chemical reactions are found to increase heat transfer rates, and this increase becomes significantly larger as Reynolds number increases.

## Nomenclature

$c_i$	Mass fraction
$c_f$	Skin friction coefficient
$e$	Internal energy/unit mass
$E_i$	Internal energy/unit vol.
$h_i$	Enthalpy/unit mass
$k$	Thermal conductivity
$k_f$	Forward rate constant
$k_b$	Reverse rate constant
$M$	Molecular weight
$M$	Collision partner
$N$	Atomic nitrogen
$N_2$	Diatomic nitrogen
$NO$	Nitric oxide
$O$	Atomic oxygen
$O_2$	Diatomic oxygen
$p$	Pressure
$q$	Heat transfer rate
$R$	Universal gas constant
$R$	Specific gas constant
$t$	Time
$T$	Temperature
$u$	x velocity component
$v$	y velocity component
$X$	Mole fraction of X
$[X]$	Concentration of X
$\gamma$	Ratio of specific heats
$\mu$	Viscosity
$\rho$	Density

## Introduction

**Question:** What are the effects of nonequilibrium chemical reactions on separated hypersonic flows? This question has not been addressed, and certainly not answered, by previous experimental, theoretical or computational investigations. However, due to the long residence time of fluid elements in a separated flow region, nonequilibrium chemical reactions may have time to progress substantially far enough such that the consequent chemical energy changes will have an effect on the structure and shape of the separated region. This work is part of an overall study at the University of Maryland to investigate this question.

There are several different geometries which can cause flow separation in hypersonic flows. Some of these include a compression corner, rearward facing step, and a shock-wave impinging on a boundary layer. The latter is the method by which flow separation was induced for the work presented here.

Hypersonic vehicles are very likely going to experience some kind of shock/boundary-layer interaction, because the shocks emanating from the nose and wing leading edges are at very shallow angles. These shocks can interact with the boundary layers along the fuselage, nacelles and other parts of the aircraft. Since hypersonic flows are characterized by very high stagnation enthalpies, the air flow around a hypersonic vehicle is chemically reacting and vibrationally excited. These chemical reactions increase local heat transfer rates making the understanding of these types of flow fields important.

Consider a Mach 25 flow which is expanded around a blunt body until the radius of curvature of the body becomes very large, and the body can be considered locally to be a flat plate. The inviscid expansion of the flow around the blunt body is considered to be a mixture of equilibrium, nonequilibrium and frozen regions (Figure 1). Figure 2 shows qualitatively the structure of a shock-wave/boundary-layer interaction on a flat plate.

\* Graduate Assistant, Student Member, AIAA  
† Professor of Aerospace Engineering, Fellow, AIAA



equations for normal stresses become:

$$\begin{aligned} \tau_{xx} &= \frac{2}{3}\mu \left( 2\frac{\partial u}{\partial x} - \frac{\partial v}{\partial y} \right) \\ \tau_{yy} &= \frac{2}{3}\mu \left( 2\frac{\partial v}{\partial y} - \frac{\partial u}{\partial x} \right) \end{aligned} \quad (6)$$

The definitions for  $\nabla q$ ,  $u_i$ ,  $v_i$ , and  $\dot{\omega}$  will be discussed later.

The rows of each vector represent respectively, the global continuity equation, the x and y momentum equations, the energy equation and the species continuity equations. The value of  $i$  ranges from 1 to 5 representing the five species included in the analysis ( $O_2$ ,  $O$ ,  $N_2$ ,  $N$  and  $NO$ ). The species continuity equations are included in the governing equations as a liberal interpretation of the Navier-Stokes equations.

The thermal equation of state for a chemically reacting gas is not a simple function of temperature as it is for a calorically perfect gas. By the use of statistical thermodynamics the sensible energy per unit mass of a species can be found. The term sensible means that the energy is measured above the zero-point energy for a particular chemical species. The zero point energy is the energy a chemical species will have if the temperature is brought down to absolute zero (0K). The equations for the sensible energy of molecules and atoms are given below [1].

$$\begin{aligned} \underbrace{e_i}_{\text{Sensible}} &= \underbrace{\frac{3}{2}R_iT}_{\text{Translational}} + \underbrace{\frac{R_iT}{2}}_{\text{Rotational}} + \underbrace{\frac{\theta_i/T}{e^{\theta_i/T} - 1}R_iT}_{\text{Vibrational}} \quad (\text{mol.}) \\ \underbrace{e_i}_{\text{Sensible}} &= \underbrace{\frac{3}{2}R_iT}_{\text{Translational}} \quad (\text{atoms}) \end{aligned} \quad (7)$$

$R_i$  is the specific gas constant of species  $i$  which can be calculated from  $R_i = R/M_i$ .  $\theta_i$  is the vibrational constant for species  $i$  and has been determined experimentally [2]. From the above equations, it can be seen that the sensible energy of a molecule consists of three energy modes while an atom has only one energy mode. Note that the electronic energy mode is neglected in the above.

The internal energy per unit mass for the gas mixture is determined by the following formulation:

$$e = \sum_i c_i \underbrace{e_i}_{\text{Sensible}} + \sum_i c_i e_{0,i} \quad (8)$$

where  $e_{0,i}$  is the zero point energy of species  $i$  and is assumed to be represented by:

$$e_{0,i} \rightarrow (\Delta h_f)_i^0 = \frac{(\Delta H_f)_i^0}{M_i} \quad (9)$$

$(\Delta H_f)_i^0$  is the "effective" zero point-energy for species  $i$ . It is in reality the heat of formation at absolute zero for species  $i$ . This is the heat of reaction of a chemical species from its "elements" at absolute zero [1]. Reference 1 gives a more detailed explanation of this.

## Chemical Source Terms

The term  $\dot{\omega}_i$  in the  $\Pi$  vector is called the chemical source term. It represents the production or destruction of a chemical species. This chemical source term is found using the following equation:

$$\dot{\omega}_i = M_i \frac{\partial [X_i]}{\partial t} \quad (10)$$

$[X_i]$  is the concentration of species  $i$ . The value of  $\frac{\partial [X_i]}{\partial t}$  is determined by the law of mass action for species  $i$ .

$$\frac{\partial [X_i]}{\partial t} = (v_i'' - v_i') \left\{ k_f \prod_j [X_j]^{v_j'} - k_b \prod_j [X_j]^{v_j''} \right\} \quad (11)$$

where  $v_i'$  and  $v_i''$  are the stoichiometric mole numbers of the reactants and products, respectively, and  $k_f$  and  $k_b$  are the forward and reverse rate constants, respectively, for a given elementary reaction. An elementary reaction is a simple reaction which takes place in a single step, i.e.,  $O_2 \rightarrow 2O$  after several collisions with other elements in the gas. The elementary reactions used in this analysis are from the modified Dunn-Kang reaction mechanism model [3]. The elementary reactions are given below:

1.  $O_2 + M \rightleftharpoons 2O + M$
2.  $N_2 + M \rightleftharpoons 2N + M$
3.  $NO + M \rightleftharpoons N + O + M$
4.  $O + NO \rightleftharpoons N + O_2$
5.  $N_2 + O \rightleftharpoons NO + N$

$M$  is defined as the collision partner which can be any of the five species used in the model. As can be seen from the above reactions, the collision partner does not change its chemical structure during the collision. The general format of the elementary reactions is shown below [1]:

$$\sum_{i=1}^5 v_i' X_i \xrightleftharpoons[k_b]{k_f} \sum_{i=1}^5 v_i'' X_i \quad (12)$$

The rate constants vary for different collision partners, but are only a function of temperature. As stated in Reference 1 the rate constants can be determined by:

$$k_f = A_f T^{B_f} e^{(-C_f/T)} \quad (13)$$

$$k_b = A_b T^{B_b} e^{(-C_b/T)} \quad (14)$$

$T$  is the temperature and  $A_f, A_b, B_f, B_b, C_f, C_b$  are constants determined from experimental data.

## Diffusion

In the present work, a multi-component diffusion model is employed. In the  $E$  and  $F$  vectors, the terms  $\rho_i u_i$  and  $\rho_i v_i$  represent the diffusion fluxes of species  $i$ .  $u_i$  and  $v_i$  are the diffusion velocity components of species  $i$  relative to the mass motion of the mixture. The diffusion velocity ( $\vec{U}_i$ ) is induced by gradients in the mass fractions of a particular species. Thermal diffusion is neglected in this analysis. The mass flux of a species is given by:

$$\vec{J}_i \equiv \rho_i \vec{U}_i = -\rho D_{im} \nabla c_i \quad (15)$$

where the right hand side of Equation 15 represents the approximation to the mass flux of a species given by Fick's Law [1].  $D_{im}$  is the multicomponent diffusion coefficient and is related to the binary diffusion coefficient of species  $i$  into  $j$  by [1].

$$D_{im} = \frac{1 - X_i}{\sum_j \frac{X_j}{D_{ij}}} \quad (16)$$

The binary diffusion coefficient is given by Equation 17.

$$D_{ij} = 0.0188293 \frac{\sqrt{T^* \left( \frac{1}{M_i} + \frac{1}{M_j} \right)}}{\rho d_{ij} \Omega_{D,ij}(T^*)} \quad (17)$$

where the units of  $D_{ij}$  are  $\text{m}^2/\text{s}$  and  $\rho$  has units of Pascals. The value of  $d_{ij}$  is approximated by  $d_{ij} = \frac{1}{2}(d_i + d_j)$ . The reduced temperature  $T^*$  is given by  $T^* = k_1 T / \epsilon_{ij}$ , where  $\epsilon_{ij} = \sqrt{\epsilon_i \epsilon_j}$ . The values for  $\Omega_d$  are tabulated. Now the components of the diffusion flux are simply calculated by:

$$\begin{aligned} \rho_i u_i &= -\rho D_{im} c_i, \\ \text{and } \rho_i v_i &= -\rho D_{im} c_i, \end{aligned} \quad (18)$$

### Heat Flux

The heat flux has several components. The first component is the energy flux due to thermal conduction:

$$\vec{q}_c = -k \nabla T \quad (19)$$

This is the same equation used for the calorically perfect gas. The only difference is in the calculation of  $k$ . For a calorically perfect gas  $k$  and viscosity,  $\mu$  are functions of temperature only, but for a chemically reacting gas they are functions of species concentrations as well as temperature. The second component is the energy flux due to diffusion. This contribution is shown below.

$$\vec{q}_D = \sum_i \rho_i \vec{U}_i h_i \quad (20)$$

where  $h_i$  is enthalpy of species  $i$  per unit mass given below.

$$\begin{aligned} h_i &= \frac{7}{2} R_i T + \frac{\theta_i/T}{e^{\theta_i/T} - 1} + (\Delta h_f)_i^0 & \text{molecules} \\ h_i &= \frac{5}{2} R_i T + (\Delta h_f)_i^0 & \text{atoms} \end{aligned} \quad (21)$$

A third contribution is due to radiation. These three contributions summed up yield the total energy flux at a point. By application of Equation 15, Equation 20 becomes

$$\vec{q}_D = \sum_i -\rho D_{im} \nabla c_i h_i \quad (22)$$

Combining Equations 19 and 22 and neglecting the contribution due to radiation, the values for the energy fluxes in vectors E and F become:

$$\begin{aligned} q_x &= -k \frac{\partial T}{\partial x} - \rho \sum_i D_{im} \frac{\partial c_i}{\partial x} h_i \\ q_y &= -k \frac{\partial T}{\partial y} - \rho \sum_i D_{im} \frac{\partial c_i}{\partial y} h_i \end{aligned} \quad (23)$$

This ends the discussion of the analytical tools used. There is no closed form solution for the governing equations so numerical techniques must be used to solve for the unknown flow variables. This is the topic of the next section.

### NUMERICAL METHOD

As stated in the previous section, the governing equations cannot be solved analytically so a numerical technique must be used. The algorithm used for the present work is MacCormack's Explicit Finite-Difference Predictor-Corrector Technique. This technique is easy to program and is proven to work well for chemically reacting flows. Only a summary of the technique will be presented here for brevity. For more details see references 4 and 5.

The MacCormack technique yields a time accurate solution of the flow problem. This means that transient, as well as steady state solutions, can be analyzed. The work presented here is for steady state solutions so transient results are not analyzed, and the initial conditions have been set to free stream values. The technique is second order accurate in time and space. That is, the truncation error due to the discretization method has a magnitude of about  $(\Delta t^2)$ ,  $(\Delta x^2)$  and  $(\Delta y^2)$ .

The solution is advanced in time to  $t + \Delta t$  using:

$$U^{t+\Delta t} = U^t + \left( \frac{\partial U}{\partial t} \right)_{AVE} \Delta t \quad (24)$$

The value of  $\left( \frac{\partial U}{\partial t} \right)_{AVE}$  is calculated by averaging the time derivatives calculated in the predictor and corrector step, i.e.,

$$\left( \frac{\partial U}{\partial t} \right)_{AVE} = \frac{1}{2} \left( \frac{\partial U^{t+\Delta t}}{\partial t} + \frac{\partial U^t}{\partial t} \right) \quad (25)$$

The derivative at time  $t$  is calculated in the predictor step and the primed derivative is calculated in the corrector step. The method for calculating these derivatives will be explained in the next two sections.

### Predictor Step

The predictor step is the first step in the MacCormack algorithm. By using forward differencing for the spatial derivatives in the governing equations, the time derivatives of the U vector at time  $t$  are found.

$$\frac{\partial U_{i,j}^n}{\partial t} = - \left\{ \frac{E_{i+1,j}^n - E_{i,j}^n}{\Delta x} + \frac{F_{i,j+1}^n - F_{i,j}^n}{\Delta y} + H_{i,j}^n \right\} \quad (26)$$

The superscript  $n$  represents values at time  $t$ , and the  $i$  and  $j$  subscripts denote the index location on the computational grid. These time derivatives are calculated only on the internal grid. All boundaries are calculated separately. (This will be discussed in detail later.) Notice that the time derivative is calculated by simply moving the E and F vectors to the right hand side of the governing equation and applying a finite-differencing scheme. This shows the time derivatives are calculated in terms of the spatial derivatives which are all known quantities at time  $n$ . The predicted values are then calculated using the time derivative as shown below.

$$U_{i,j}^{n+1} = U_{i,j}^n + \frac{\partial U_{i,j}^n}{\partial t} \Delta t \quad (27)$$

The prime denotes the predicted value at time  $t + \Delta t$  (or the  $n+1$  time level).

### Corrector Step

The time derivative in the corrector step is calculated by using a rearward differencing scheme for the spatial derivatives. Equation 28 shows how the corrector step time derivative is calculated.

$$\frac{\partial U_{i,j}^{n+1}}{\partial t} = - \left\{ \frac{E_{i,j}^{n+1} - E_{i,j}^{n+1}}{\Delta x} + \frac{F_{i,j}^{n+1} - F_{i,j}^{n+1}}{\Delta y} + H_{i,j}^{n+1} \right\} \quad (28)$$

The values of the various vectors used on the right hand side are the values calculated in the predictor step by Equation 27. The values of  $E_{i,j}^{n+1}$  can now be calculated using Equations 24 and 25.

### Numerical Dissipation

In order to achieve stable solutions in the areas of high pressure gradients, a product fourth-order damping term  $\Delta U_{ij}$  [6] is added to the right hand side of Equations 26 and 24 during the predictor and corrector steps, respectively. The calculation of  $\Delta U_{ij}$  is shown below.

$$\Delta U_{i,j} = (\Delta U_{i,j})_x + (\Delta U_{i,j})_y \quad (29)$$

where

$$(\Delta U_{i,j})_x = c_x \frac{[p_{i+1,j} - 2p_{i,j} + p_{i-1,j}]}{[p_{i+1,j} + 2p_{i,j} + p_{i-1,j}]} \cdot [U_{i+1,j} - 2U_{i,j} + U_{i-1,j}]$$

$$\text{and } (\Delta U_{i,j})_y = c_y \frac{[p_{i,j+1} - 2p_{i,j} + p_{i,j-1}]}{[p_{i,j+1} + 2p_{i,j} + p_{i,j-1}]} \cdot [U_{i,j+1} - 2U_{i,j} + U_{i,j-1}]$$

The coefficients  $c_x$  and  $c_y$  range from 0.0 to 0.5. This is a compact explicit method since only the adjacent nodes are needed to calculate the dissipation. This compactness leads to a better resolution of shocks than is obtained from other fourth-order schemes which require more points [6]. Artificial dissipation eliminates truncation errors which result in the solution being only second order accurate. As grid density is increased, the effects of numerical dissipation become less since their contribution is of  $O(\Delta x^4, \Delta y^4)$ . As stated in Reference 6, this method of dissipation works very well for shocks in high Mach number flows. This is a very important factor, because there are several strong shocks in the flows studied in this investigation.

### Boundary Conditions

For the cases treated in the present paper, it has been discovered through trial and error that boundary conditions play a very important role in obtaining a stable and correct solution. The boundary conditions listed in this section are the conditions found to yield stable "accurate" solutions. The term "accurate" refers to solutions matching those obtained by theory and other codes.

The only boundary which is never updated is the inflow boundary. The flow and chemistry variables are held constant

at the inflow boundary (consistent with a supersonic inflow), and are set equal to values obtained as follows.

The inflow conditions are calculated by assuming air at an altitude of 61 km is processed by a Mach 25 normal shock and then expanded around an arbitrary blunt body to the Mach number of interest. The equilibrium flow conditions behind a Mach 25 normal shock are obtained from Reference 7 and are used as starting conditions for the expansion. Through the expansion, the gas mixture is assumed to be "frozen", that is, non-reacting. With this assumption and the assumption that the gas is isentropically expanded, inlet conditions to the flat plate are obtained.

In general the numerical dissipation coefficient has to be relatively low for a chemically reacting analysis. By trial and error a value of 0.10 is found to yield stable solutions. Values any higher than this cause instabilities and eventual departure of the solution. For the calorically perfect gas flows, the coefficients can be much higher, and in fact, for a stronger shock they have to be set to values of 0.25 so stable solutions can be achieved.

### Plate (Wall) Boundary

Along the wall, the velocity is held constant at zero to satisfy the no-slip boundary condition. For the cases presented, the wall temperature is set equal to the free stream temperature. This is known as a "cold" wall since the fluid temperature right above the wall is much higher due to viscous effects. Pressure is calculated by performing a linear extrapolation normal (y-direction) to the plate as shown below.

$$p_{i,1} = 2p_{i,2} - p_{i,3} \quad (31)$$

The plate is considered to be non-catalytic, i.e.,  $(\partial c_i / \partial n)_w = 0$ , so the species mass fractions are set equal to those of the next row of grid points away from the plate  $((c_i)_{i,1} = (c_i)_{i,2})$ . The case for a catalytic wall is treated by Grumet et al [9].

A fourth order polynomial fit [5] is used to calculate the y-derivatives for the diffusion terms in Equations 5, 6 and 23. These are the shear stress and two heat transfer equations, respectively. The fourth order polynomial fit is given in Equation 32 where the term  $f$  is replaced by  $u$  for calculating shear stress and  $T$  for calculating heat transfer.

$$\left( \frac{\partial f}{\partial y} \right)_{i,1} = \frac{1}{12\Delta y} [-25f_{i,1} + 48f_{i,2} - 36f_{i,3} + 16f_{i,4} - 3f_{i,5}] + O(\Delta y^4) \quad (32)$$

A fourth-order scheme is used for accuracy, and because the temperature profiles near the wall have a high curvature. This high order scheme is found to yield good results when surface skin friction and heat transfer rates at the wall calculated by the computer code are compared to the reference temperature method of reference 1.

### Outflow Boundary

The outflow conditions are treated mainly as a supersonic outflow, and hence are calculated using linear extrapolations

in the x-direction for pressure, temperature and velocities. All other flow variables are calculated from these extrapolated values. As with the wall boundary, there is a zero gradient in the mass fractions out the rear boundary.

Special care is taken in the region of subsonic flow in the exit flow plane. Pressure is not extrapolated here, but rather, it is set equal to the pressure where the flow reaches sonic conditions at the exit plane. This is done since the Navier Stokes equations become elliptic in subsonic regions, and the upstream flow is affected by what is happening downstream.

#### Upper Boundary

The upper boundary is treated essentially the same as the outflow boundary with the exception that the extrapolation is in the y-direction. In addition, in the region where the shock boundary conditions are imposed, usually along the first 5 to 10 grid points on the upper boundary, pressure and temperature are held constant at prescribed values (dependent on shock strength desired). The velocities are extrapolated in this region in the same manner as for the rest of the upper boundary, and the other flow variables are then calculated.

For the chemical species, the mass fraction is once again held constant in the normal direction. This condition however, is not imposed in the shock region. In the shock region, the mass fractions are held at a constant value equal to the free stream values. This is done because flow through a shock is "frozen". The chemistry boundary condition is usually held at fewer grid points than the pressure and temperature conditions.

#### CODE VALIDATION

Since there are no analytical solutions to the governing equations, code validation is done by comparing results obtained through this analysis to those obtained using other codes and to the results obtained using the reference temperature method [1].

When the computer code is run without an impinging shock, the heat transfer rates to the wall and skin friction calculated can be compared to the reference temperature method. When this is done, the difference between the analytical and computational values is less than 2%.

Another method used to validate the code is a check on grid convergence. Grid densities of 30x40, 40x50 and 50x70 are used to determine grid convergence. When these three densities are used for the same flow conditions, velocity profiles at the mid-plate location and plate trailing edge location were found to be nearly the same for the three grids [8]. All low Reynolds number cases (1-6) are done on a 40 x 50 grid to be sure there were enough grid points in the y-direction to accurately describe conditions near the wall and reduce computer time.

Since no experimental data for low Reynolds number shock/boundary-layer flows could be found, a direct comparison to the results obtained using Adam Grumet's [9]<sup>2</sup> code is done. Solutions after 3,500 and 10,000 timesteps from both codes are in very close agreement. A maximum difference in the heat transfer rate to the wall is found at the reattachment

point. The difference is 2% [8]. The very good agreement in results is a good indication that both codes are calculating the flow field accurately. This is especially true since both codes were developed independently.

#### Steady State

Obtaining a steady state solution is very difficult for this separated flow problem. After letting a solution proceed to 20,000 timesteps, a cutoff limit of 9,000 timesteps was determined. A difference in solutions exists between the two time periods, but the difference is very small (2%). This difference is found to be acceptable for the studies presented. Work done by Grumet has indicated that even after 40,000 timesteps the flow is still changing slightly. This may indicate that a steady state solution may not be obtainable in a timely and cost effective manner.

#### RESULTS AND DISCUSSION

In this section the results of various analyses will be presented. Unless otherwise stated the Reynolds number based on plate length and free stream conditions for all analyses is 1500 for calorically perfect flows and 1573 for chemically reacting flows. These Reynolds numbers were chosen to be intentionally low in order to have reasonable run times on the computer. The Reynolds numbers based on the location where an inviscid calorically perfect shock would impinge on the plate are 750 and 786 for the two types of flows, respectively. Table 1 shows the free stream conditions for Mach 5 and Mach 12. As stated previously, the free stream conditions were arrived at by processing a Mach 25 flow through a normal shock and isentropically expanding the frozen flow to the desired Mach number.

Table 1 — Free stream Conditions

Freestream	Mach 5	Mach 12
u (m/s)	4891.02	5466.12
p (Pa)	57.884	19.17
T (K)	1130.34	245.10
R (J/kg K)	515.25	515.25
gamma	1.60	1.62
CO <sub>2</sub>	0.0	0.0
CO	0.2675	0.2675
CN <sub>2</sub>	0.1971	0.1971
CN	0.5354	0.5354
CNO	0.0	0.0
Plate length (m)	0.13770	0.02846

The values for R and  $\gamma$  in Table 1 are the ones used to obtain a calorically perfect gas solution. These values are calculated using the mass fractions and the free stream temperature given in Table 1. The plate temperature is set equal to the free stream temperature so the dimensionless hypersonic parameter  $T_w/T_\infty$  is unity.

Shock strength is determined by picking a shock angle ( $\beta$ ) and using the oblique shock relations with the proper value of

<sup>2</sup> Adam Grumet is a graduate student at the University of Maryland, 1990.

gamma [2] The values for the pressure and temperature ratios will be given for each Mach number in the following sections.

To speed up the analyses, the code which calculates flows for a calorically perfect gas is first run to 4,000 time steps. The flow field generated after these 4,000 time steps is used for the initial conditions of the chemically reacting code. This yields a savings in cpu time since the calorically perfect code runs two to eight times faster than the chemically reacting code. In Table 2 below are the various run times for the two codes on the IBM mainframe and the JPL CRAY-XMP.<sup>1</sup>

Table 2 — Computer run times

CODE	IBM	CRAY
Calorically Perfect	61	238
Chemically Reacting	5/15*	51/94*

The numbers listed in Table 2 represent the number of time steps per cpu minute each machine can perform. The interactive run times for the codes were 2X and 5X for the IBM and CRAY, respectively.

Care should be taken when looking at plots. The plot distances in the x and y directions are not proportionally correct. The results are presented in this manner for visual clarity.

Four Mach 5 cases and three Mach 12 cases have been completed. The shock strengths analyzed are shown in Tables 3 and 4. The third Mach 12 case (Case 7) is a high Reynolds number flow and the results will be discussed later.

Table 3 — Mach 5 Induced Shock Strength's

Case (angle)	Pressure Ratio	Temperature Ratio
Case 1 (25)	5.265	2.122
Case 2 (28)	6.551	2.426
Case 3 (30)	7.461	2.640
Case 4 (32)	8.410	2.862

Table 4 — Mach 12 Induced Shock Strengths

Case (angle)	Pressure Ratio	Temperature Ratio
Case 5 (30)	44.282	11.418
Case 6 (35)	58.349	14.748

The shock strengths in Table 3 are those which yield separated flows. For shock strengths less than Case 1, the flow will not separate, and for shock strengths greater than Case 4, a Mach reflection will result. Similarly, Cases 5 and 6 bracket the shock strengths for separated flows at Mach 12. Artificial dissipation coefficients are equal for both calorically perfect and chemically reacting cases. This statement does not apply to Cases 4 and 6 where the incident shock is very strong. The coefficients have to be increased from 0.10 to 0.20 for the

calorically perfect flow. The value for the chemically reacting flow is still 0.10.

Figure 3 shows a typical pressure contour plot. In this plot, the various shocks and expansion wave discussed earlier can be seen. Figure 4 is a temperature contour plot which shows the large region of relatively cool temperatures in the separation region. A velocity vector diagram is given in Figure 5. The solid lines represent the calorically perfect inviscid incident and reflected shock locations. The separated region is indicated by arrows pointing in an upstream direction (left).

The main reaction taking place in the separation region and the rest of the flow field is the formation of  $N_2$  from  $N$ . Figure 6 shows a contour plot of  $N_2$ . This formation results in an energy release which can be seen in the form of temperature in Figure 7. The temperature plotted in Figure 7 is the gas temperature one row of grid points above the plate. This increased temperature results in an increase in pressure and heat transfer to the plate (Figures 8 and 9).

These increases are present in all cases, and as shock strength increases, the amount of formation of  $N_2$  also increases. Some other flow parameters are tabulated in Table 5.

Figure 3 — Pressure Contour (Pa) — Case 3: Mach 5,  $Re=1,500$  with a  $30^\circ$  incident shock

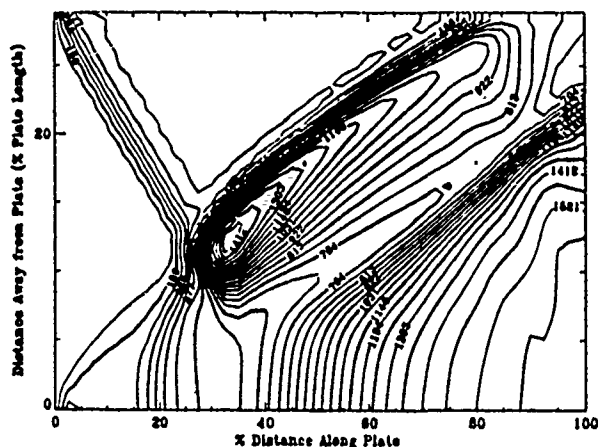
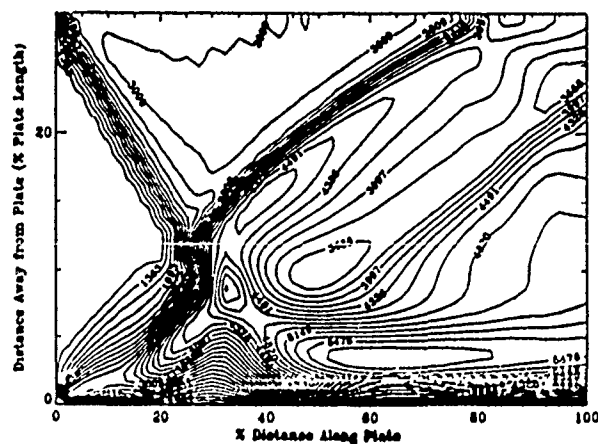


Figure 4 — Temperature Contour (K) — Case 3: Mach 5,  $Re=1,500$  with a  $30^\circ$  incident shock



<sup>1</sup> In the second row the starred numbers are the number of iterations per cpu minute needed to run the code when transport properties are calculated every fifth time step.

Figure 5 — Velocity Vector Diagram — Case 3: Mach 5,  $Re=1,500$  with a  $30^\circ$  incident shock

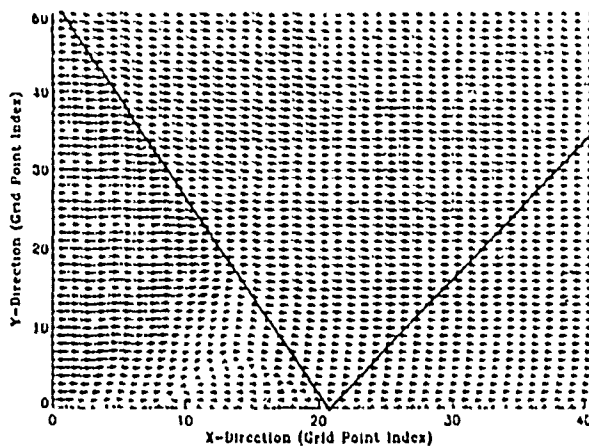


Figure 8 — Surface Pressure Distribution — Case 3: Mach 5,  $Re=1,500$  with a  $30^\circ$  incident shock

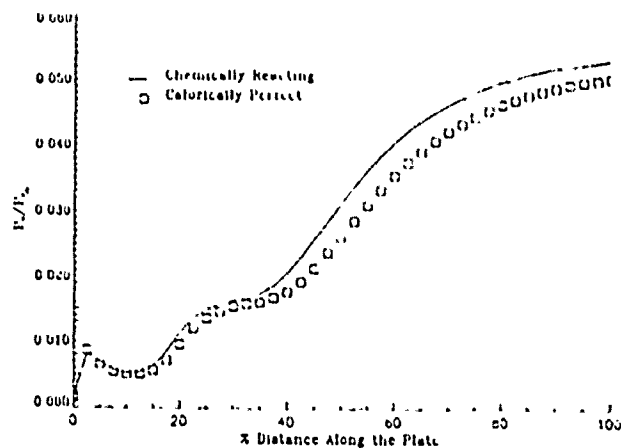


Figure 6 —  $N_2$  Mass Fraction Contour — Case 3: Mach 5,  $Re=1,500$  with a  $30^\circ$  incident shock

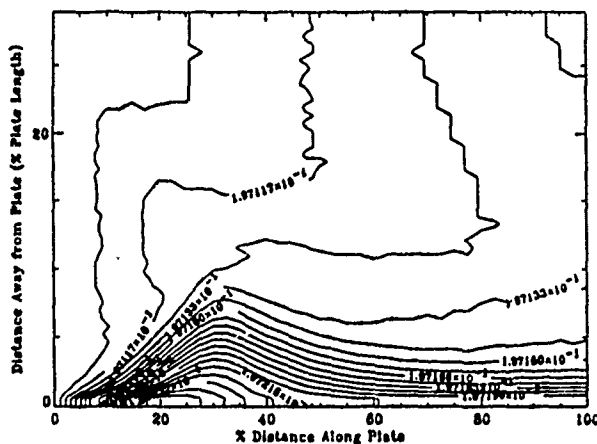


Figure 9 — Heat Transfer Rates to Plate — Case 3: Mach 5,  $Re=1,500$  with a  $30^\circ$  incident shock

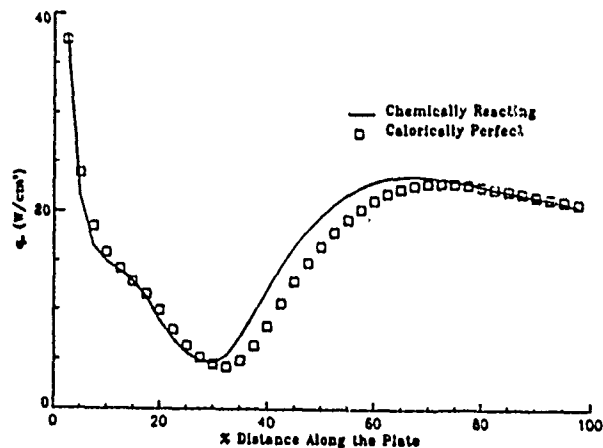


Figure 7 — Temperature Near Surface — Case 3: Mach 5,  $Re=1,500$  with a  $30^\circ$  incident shock

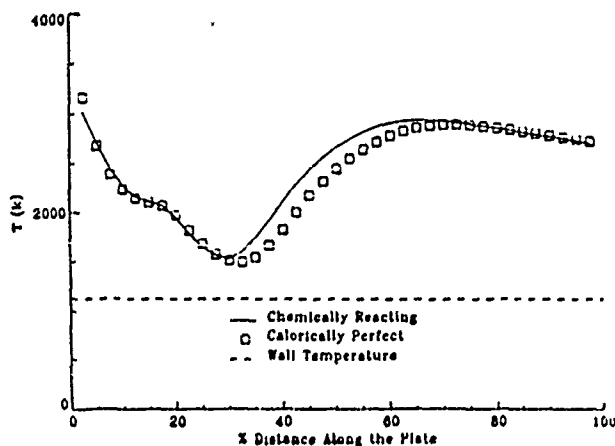


Table 5 — Parameter Summary

	Case 1	Case 2	Case 3	Case 4	Case 5	Case 6
Length	8%	23%	32%	40%	9%	37%
$q_{max}$	20.54	22.65	23.6	22.3	60.7	52.86
$P_{max}$	0.034	0.045	0.055	0.051	0.40	0.47
Max $T_{gas}$	2432	2794	2945	2989	2670	2828
$Re_{sep}$	550	346	314	252	550	283
$Re_{reatt}$	676	739	818	880	692	865
$\Delta q_{max}$	3.3%	3.8%	3.0%	2.0%	3.1%	7.0%
$\Delta P_{max}$	0.1%	0.4%	0.5%	0.6%	4.0%	6.0%

Many notable features of the separated flow can be found in Table 5. One of these is the rapid increase in separation bubble size. This region grows in a nearly linear manner with increasing shock strength. In the first row of Table 5 the lengths of the separation regions are given in percent of the plate's length. Heat transfer also increases with shock strength. The units of heat transfer in Table 5 are  $W/cm^2$ . For the very strong shock solutions (Cases 4 and 6), the wall heat transfer actually decreases slightly even though the gas temperature near the plate is higher. This is due to the temperature profiles at the peak heat transfer locations being flatter. That is, the gradient in temperature past the first row of grid points is lower for the stronger shock solutions. This lower gradient is accounted for by using the fourth order polynomial fit (Eq. 32) in calculating heat transfer to the wall.

As shock strength is increased the separation point Reynolds number continually decreases and the reattachment point Reynolds number steadily increases. These Reynolds numbers are based on free stream conditions and location on the plate. For the first two cases the reattachment point is ahead of the inviscid shock impingement location, and for cases 3 and 4 the reattachment point is downstream of the impinging shock location. The use of the inviscid shock location is for reference purposes only. The same result is seen for the Mach 12 cases. The weaker shock case has a reattachment point upstream of the impinging shock location, and the stronger shock case reattachment point is downstream of the shock location. For both the Mach 5 and Mach 12 cases where the reattachment point is further downstream, the distance away from the inviscid incident shock location is small.

The pressures listed are the maximum pressure on the plate (leading edge excluded) non-dimensionalized by the free stream total pressure. The surface pressure behind the incident shock increases proportionally with increased shock strength as is expected. The increase in non-dimensional pressures for the Mach 12 cases are a magnitude greater than the Mach 5 cases.

The last two rows of Table 5 show the percent differences between the chemically reacting and the calorically perfect flows for maximum heat transfer and surface pressure. For Cases 1 through 5 the differences in heat transfer range from 2% to 4%. Case 6 has the largest difference at 7%. The difference between maximum pressure is increased the most when the Mach number is raised. The difference between the chemically reacting and calorically perfect flows increases by a factor of 10 when the Mach number is raised from 5 to 12. The difference in heat transfer rates are less effected by increasing Mach number (factor of 2 increase).

#### HIGH REYNOLDS NUMBER CASE

A high Reynolds number case is presented, because it is believed that the effects of chemical reactions will become much greater as Reynolds number is increased. In this section are the results of a Mach 12 flow with a  $30^\circ$  incident shock. The Reynolds number is 16,000. The two input parameters which are changed to increase the Reynolds number are pressure and plate length. Their values are 80 Pa and 0.0683 m, respectively, compared to the previous values of 19.17 Pa and 0.02846 m.

The increase in pressure is necessary since only increasing the plate's length causes the computer run to crash. This is due to the cell Reynolds number becoming too large for a given grid size. The explicit nature of MacCormack's technique is the reason for instabilities which arise when high cell Reynolds numbers occur. (This unstable nature is the reason for the bulk of the present work being done at low Reynolds numbers.) For the first six cases, the maximum cell Reynolds in the x-direction is 50, but for the case presented here, the maximum cell Reynolds number in the x-direction number is greater than 400. This high value causes many instabilities and the values for artificial viscosity coefficient and CFL number have to be changed from time to time to continue advancing the solution in time. A similar trend occurs with the cell Reynolds number in the y-direction. The artificial viscosity coefficient and CFL number for the calorically perfect flow are 0.2 and 0.6, respectively. The values for the chemically reacting flow range from 0.1 to 0.25 and 0.20 to 0.30 respectively for the artificial viscosity coefficient and CFL number.

In Table 6 various flow parameter are listed for the two Reynolds number cases.

Table 6 — High Reynolds Number Results

Parameter	Re=16,000	Re=1,500
$q_{max}$	65.5	60.7
$T_{max}$	5257	2670
$P_{max}$	0.455	0.400
Delta $q_{max}$	14.6%	3.1%
Delta $P_{max}$	9.4%	4.0%

As was expected the differences between the chemically reacting flow and the calorically perfect flow increased dramatically with the increase in Reynolds number. It can be seen that the difference between the maximum heat transfer rates for the chemically reacting and calorically perfect flows has increased by a factor of almost five (fourth row of Table 6.) This increased difference shows that chemical reactions are becoming more important as Reynolds number is increased. The difference between maximum pressure is also greater for the high Reynolds number case.

Figures 10 through 16 show the results for this high Reynolds number case. The difference between wall shear stress for the chemically reacting and calorically perfect flows is quite noticeable downstream of the reattachment point (Fig. 10). The increase in shear stress for a chemically reacting flows is an expected result which is not very evident for the low Reynolds number cases. Figure 11 shows the separation region is much larger for the high Reynolds number case. This is due to the fact that the boundary layer is much thicker<sup>4</sup> and has less momentum further from the plate to overcome separation. This larger separation region allows not only  $N_2$  to form as in Case 5, but  $O_2$  is now able to form (Figures 12 and 13). For Case 5, there is no  $O_2$  in the separation region. The mass fraction for  $N_2$  has increased by 8.2%. The increase for Case 5 is less than 1.0%. The increased amount of formation

<sup>4</sup> The increased boundary layer thickness is due to the increase in the absolute scale of the flow for the higher Reynolds number flow. The plate length and grid height are more than double the lower Reynolds number case.

of both  $N_2$  and  $O_2$  is the reason for the increased heat transfer rates to the plate and increased pressure on the plate.

Figure 10 — Plate Shear Stress Case 7:  
Mach 12,  $Re=16,000$  with a 30° incident shock

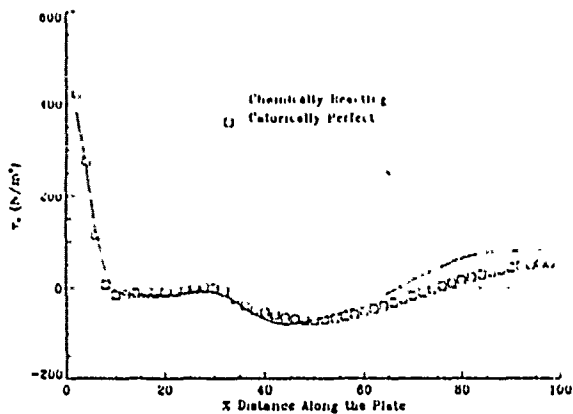


**Figure 11 — Velocity Vector Diagram — Case 7:  
Mach 12,  $Re=16,000$  with a  $30^\circ$  incident shock**

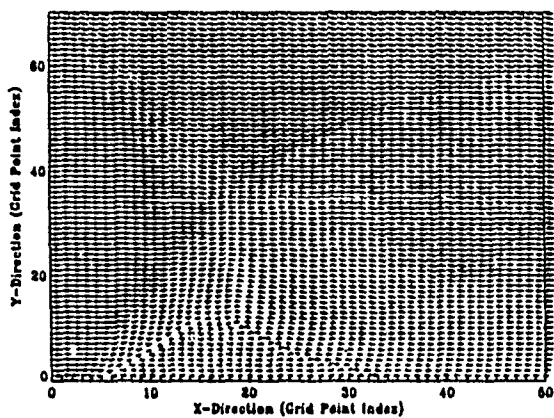


Figure 12 —  $N_2$  Mass Fraction Contour — Case 7: Mach 12,  $Re=16,000$  with a  $30^\circ$  incident shock

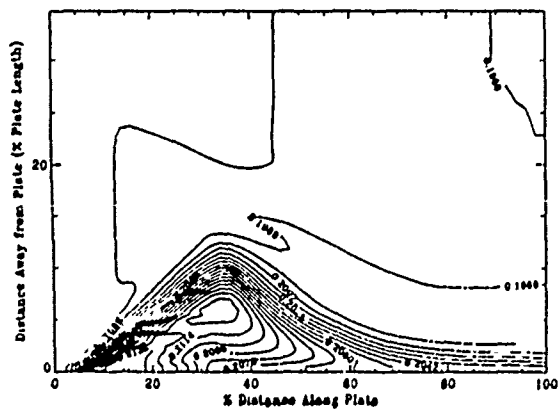
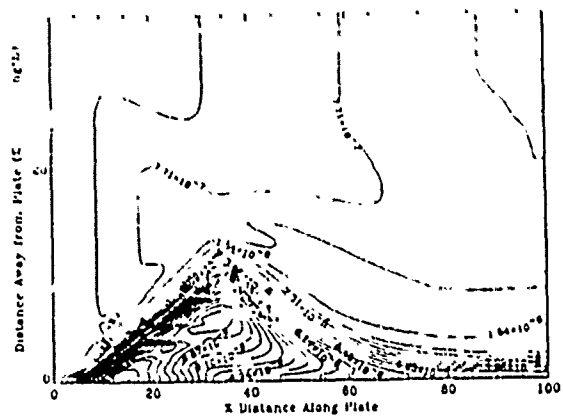
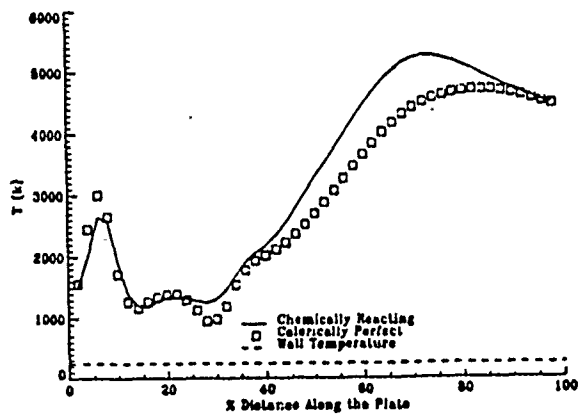


Figure 13 —  $O_2$  Mass Fraction Contour — Case 7, Mach 12,  $Re=16,000$  with a  $30^\circ$  incident shock



The energy release due to the formation of  $N_2$  and  $O_2$  results in a large increase in gas temperature near the plate surface (first row of grid points above the plate). The maximum temperature near the plate for the chemically reacting flow is 560K higher than the calorically perfect flow (Fig. 14). Figures 15 and 16 show the increase in pressure distribution and heat transfer rates, respectively.

Figure 14 — Temperature Near Surface — Case 7: Mach 12,  $Re=16,000$  with a  $30^\circ$  incident shock



**Figure 15 — Surface Pressure Distribution — Case 7: Mach 12,  $Re=16,000$  with a  $30^\circ$  incident shock**

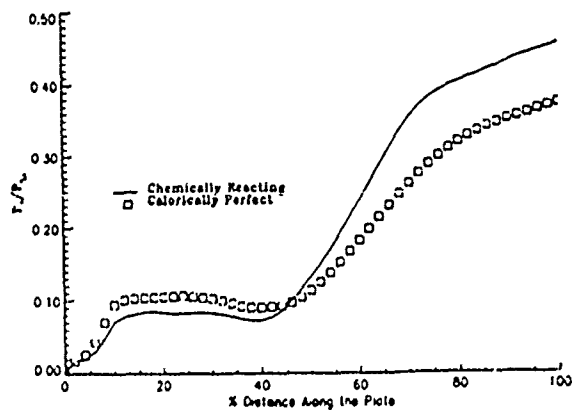
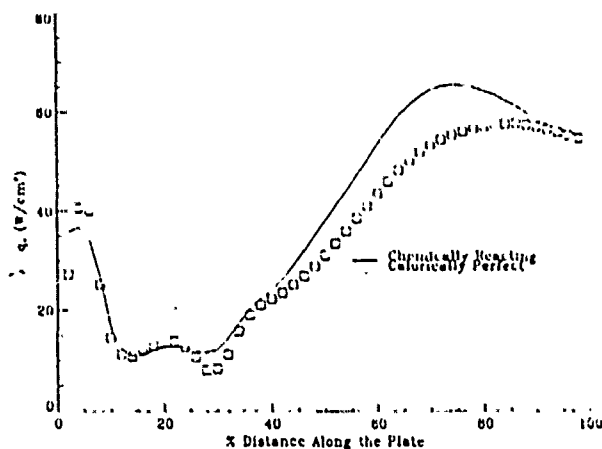




Figure 16 — Heat Transfer Rates to Plate — Case 7: Mach 12,  $Re=16,000$  with a  $30^\circ$  incident shock



Further work on high Reynolds number cases was not possible using the code which was used for the work presented here. The reasons for this are stated at the beginning of this section. All the trends listed for the low Reynolds number cases are expected for higher Reynolds numbers with the differences between chemically reacting and calorically perfect gases becoming much greater.

### Conclusions

The effects of chemical reactions on the magnitudes of heat transfer and pressure distribution are moderate for the low Reynolds number flows analyzed. Since the effects of chemical reactions are moderate, the flow can be modeled with a fair degree of accuracy for preliminary designs using calorically perfect gas assumptions (with the proper gas constant and ratio of specific heats for the composition of the gas being analyzed). These assumption, however, begin to breakdown as the shock strength approaches a value which will cause a Mach reflection.

When the Reynolds number is increased, the effects of chemical reactions become substantially greater, and the differences between the reacting flow and calorically perfect flow become very large. Any hypersonic vehicle designed in the future is very likely going to fall in the category of high Reynolds number flows rather than very low Reynolds number flows.

Chemical reactions will have to be accounted for somewhere in the design process since they do increase both heat transfer rates and pressure on the plate. Also, chemical reactions have an effect on the location of both maximum heat transfer and pressure. Both the increase and change of location can be important factors in the design of hypersonic vehicles.

The following conclusions can be made about the effects of shock strength on non-equilibrium chemically reacting separated flows in the shock-wave/boundary-layer interaction region. These are all expected results.

- Heat transfer to the plate generally increases except for a strong shock which will not cause a Mach reflection. In this case, the heat transfer actually drops because the

variation of temperature in the normal direction to the plate is lower than for shocks of lower strengths.

- Surface pressure increases behind the reattachment point.
- The size of the separation bubble increases substantially with increased shock strength.
- The separation point moves forward on the plate due to the increased adverse pressure gradient with increased shock strength.
- The reattachment point moves down stream as shock strength is increased.

These results demonstrate that nonequilibrium chemical reactions can have an effect on high enthalpy hypersonic separated flows, and hence further investigations of such flows should take such effects into account.

### ACKNOWLEDGEMENTS

This work was supported in part by AFOSR Grant No. 88.0101 with James Wilson and Len Sakell as grant monitors, and by NASA Ames Grant No. NAG-2-529 with George S. Deiwert as grant monitor. Also, the support of the Computer Science Center at Maryland is gratefully acknowledged for providing some of the computer resources and time for these calculations, as well as the Jet Propulsion Laboratory for providing CRAY time. Finally, the authors gratefully acknowledge the supportive conversations of the graduate students and Dr. Mark Lewis, Assistant Professor, all members of the Hypersonic Aerodynamics Research Group at Maryland.

### REFERENCES

1. Anderson, John D., Jr., Hypersonic and High Temperature Gas Dynamics, New York, McGraw-Hill-Book Co., 1989.
2. JANAF Thermochemical Tables, 2nd Edition, edited by D. R. Stall and H. Prophet, NSROC-NBS 37, June, 1971, QC 100.U537.
3. Gnoffo, P. A., and McCandless, R. S., "Three-Dimensional AOTV Flow fields in Chemical Nonequilibrium," AIAA-86-0230, January, 1986.
4. Anderson, John D., Jr., Modern Compressible Flow, New York, McGraw-Hill Book Co., 1982.
5. Anderson, Dale A., Tannehill, John C., and Pletcher, Richard H., Computational Fluid Mechanics and Heat Transfer, New York, McGraw-Hill Book Co., 1984.
6. Hung, C. M., McCormack, R. W., "Numerical Solutions of Supersonic and Hypersonic Laminar Corner Flows," *AIAA Journal*, Vol. 14, No. 4, April 1976, pp. 475-481.
7. Erickson, Roy W., "The Non-Equilibrium Chemistry Behind a Mach 25 Normal Shock," Internal Report, University of Maryland, Department of Aerospace Engineering, 1989.
8. Ballaro, Charles A., "Shock Strength Effects on Separated Flows in Non-Equilibrium Chemically Reacting Air — Shock Wave/Boundary Layer Interaction," UM-AERO-90-16, Thesis for MS Degree at the University of Maryland, 1990.
9. Grunet, Adam, Anderson, John D., Jr., "A numerical Study of the Shock Wave Boundary Layer Interaction in Nonequilibrium Chemically reacting Air: The Effects of Catalytic Walls," AIAA-91-0245, January, 1991.

## Appendix B

# A Numerical Study of the Shock Wave / Boundary Layer Interaction in Nonequilibrium Chemically Reacting Air: The Effects of Catalytic Walls

by

Adam A. Grumei\*  
Dr. John D. Anderson Jr.†  
and  
Dr. Mark J. Lewis‡

Department of Aerospace Engineering  
University of Maryland  
College Park, MD 20742

## Executive Summary:

This work is the *first* study of the effects of nonequilibrium chemically reacting flow on the generic problem of a hypersonic shock wave / boundary layer interaction. This paper *also* includes the effects of catalytic walls. Results have shown that the inclusion of catalytic surfaces drastically increases the wall heat transfer and must be accounted for. This work should be of interest to all investigators dealing with high enthalpy hypersonic flows.

## 1 Introduction

During the past decade, there has been a resurgence of interest in the design of hypersonic vehicles, driven by the successful Space Transportation System (Space Shuttle), the National AeroSpace Plane (NASP) and others. Interest has focused not only on the overall design of hypersonic vehicles, but on detailed fluid dynamic and thermodynamic problems associated with the high speed flight regime. One major hurdle that must be overcome for the feasible design of a transatmospheric vehicle is an accurate prediction of surface heat transfer. Because hypersonic vehicles experience much larger heat transfer rates than conventional supersonic aircraft, structures will likely be stressed to their performance limits even with the advent of new high temperature materials. It is likely that active cooling mechanisms will

---

\* Research Assistant, Student Member, AIAA

† Professor of Aerospace Engineering, Fellow, AIAA

‡ Assistant Professor of Aerospace Engineering, Member, AIAA

be required for transatmospheric flight. Undoubtedly there will be great weight restrictions on these cooling mechanisms. Therefore the *accuracy* of the prediction of the surface heat transfer is paramount.

Among the many different heat transfer problems encountered during hypersonic flight, one of the most significant will be the very large local peaks of heat transfer that can occur in the region where an oblique shock wave impinges upon a boundary layer. This interaction is inevitable; for scramjet propulsion, incident oblique shock waves will be reflected inside the engine diffuser from the cowl lip, as shown in figure 1.

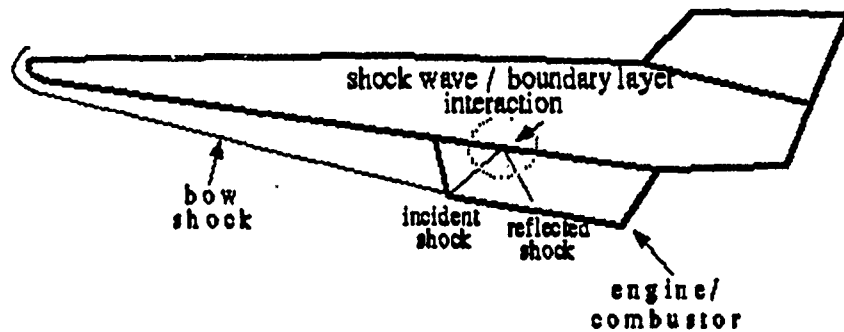


Figure 1 Schematic diagram of reflecting shocks inside the engine of a hypersonic vehicle

The adverse pressure gradient caused by an incident oblique shock on a boundary layer can separate the flow upstream of the impingement point. Subsequently, the boundary layer is lifted from the plate surface and reattaches downstream behind the separated region. It is at this point of reattachment that the heat transfer is highest. A schematic diagram of the shock wave / boundary layer interaction is shown in figure 2. It is this interaction that will be the primary focus of this paper.

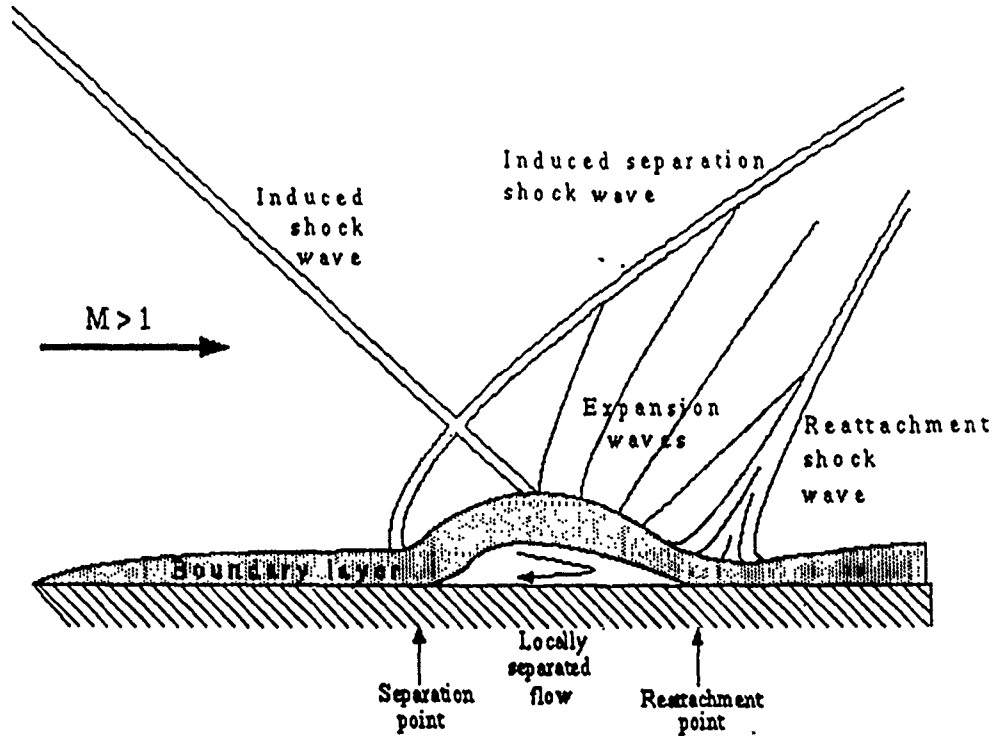


Figure 2 Schematic diagram of separated flow due to oblique shock wave boundary layer interaction

## 1.1 Past Work

Because of the importance of the shock wave / boundary layer problem, and separated flow in general, there is an extensive volume of past work done in this area, both experimental and numerical<sup>1</sup>. As early as the late 1940's, Goldstein (1948) performed experiments to study the separation of laminar flow. In 1954, Bogdonoff and Kepler studied the separation of supersonic turbulent flow. In the 1970's, with the advent of computational fluid dynamics, *numerical* investigations of laminar separation were possible. Both Issa and Lockwood (1977) and Hodge (1977) predicted supersonic and hypersonic laminar shock wave / boundary layer interactions. These numerical investigations were to become more involved in the 1980's including such complexities as turbulent modeling and three dimensional flows. In 1987, Hoestman calculated a hypersonic shock wave / *turbulent* boundary layer interaction, and Gaintonde and Knight (1988) performed numerical experiments on *three dimensional*

shock wave / boundary layer interactions. Most recently <sup>2</sup>, Bogdonoff (1990), numerically modeled a *three dimensional* shock wave interacting with a *turbulent* boundary layer. However, to the authors' knowledge, no previous work has been done to numerically investigate the shock wave / boundary layer interaction and *include the effects of nonequilibrium chemistry*, especially with catalytic surfaces. This is the goal of the present work.

## 1.2 Present Study

This paper will consider the frozen flow of air that enters the scramjet inlet after it has been expanded around the forebody of a hypersonic vehicle. The oxygen will be entirely dissociated and the nitrogen will also be dissociated to some degree. Inside the separation region, where the flow is recirculating, a large amount of chemical recombination will occur, thus releasing energy. This may, in turn, increase the heat transfer considerably. Furthermore, if the recombination is accelerated due to catalytic effects at the wall, *the heat transfer may be even higher*.

This paper considers the effects of non-equilibrium chemical reactions as well as wall catalycity on hypersonic shock wave / laminar boundary layer interactions and compares the results with those obtained from a nonreacting (calorically perfect) flow.

## 2 Computational Solution

### 2.1 Governing Equations

For this paper, the aforementioned physical problem was modeled by numerically solving the full Navier-Stokes equations for nonequilibrium chemically reacting air. The Navier-Stokes equations in strongly conservative form is shown below

$$\frac{\partial \vec{U}}{\partial t} + \frac{\partial \vec{E}}{\partial x} + \frac{\partial \vec{F}}{\partial y} = \vec{J}$$

Where the vectored variables are

$$\vec{U} = \begin{Bmatrix} \rho \\ \rho u \\ \rho v \\ \rho \left( e + \frac{V^2}{2} \right) \\ \rho c_i \end{Bmatrix}$$

$$\vec{E} = \begin{Bmatrix} \rho u \\ \rho u^2 + p - \tau_{xx} \\ \rho uv - \tau_{xy} \\ \rho \left( e + \frac{V^2}{2} \right) u + pu - q_x - u\tau_{xx} - v\tau_{xy} \\ \rho c_i u - \rho D_{im} \frac{\partial c_i}{\partial x} \end{Bmatrix}$$

$$\vec{F} = \begin{Bmatrix} \rho v \\ \rho uv - \tau_{yx} \\ \rho v^2 + p - \tau_{yy} \\ \rho \left( e + \frac{V^2}{2} \right) v + pv - q_y - u\tau_{yx} - v\tau_{yy} \\ \rho c_i v - \rho D_{im} \frac{\partial c_i}{\partial y} \end{Bmatrix}$$

$$\vec{J} = \begin{Bmatrix} 0 \\ 0 \\ 0 \\ 0 \\ \dot{w}_i \end{Bmatrix}$$

The chemically reacting Navier - Stokes equations differ from its calorically perfect counterpart in that the species continuity equation is included. In the non-conservative differential form, the species continuity equation is given as

$$\frac{Dc_i}{Dt} = \dot{w}_i + \nabla \cdot (\rho D_{im} \nabla c_i)$$

This equation states that the time rate of change of the mass of species  $i$  is due not only to the species convection, but two additional terms must be included as well, namely:

1. The chemical source term,  $\dot{w}_i$ , which is the local rate of change of  $\rho c_i$  due to chemical reactions.

2. The chemical diffusion term, which is the flux of species  $i$  due to a local gradient of that species.

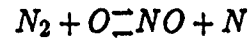
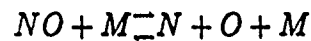
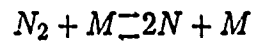
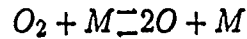
The species continuity equation is solved independently for each species  $i$ .

### Chemical rate equations

The chemical source term found in the species continuity equation is given as

$$\dot{w}_i = M_i \frac{d[X_i]}{dt}$$

For the following elementary reactions



the reaction rate constants,  $k_f$  and  $k_b$ , are determined from Arrhenius' equation

$$k_f = A_f T^{B_f} e^{-\frac{C_f}{T}}$$

$$k_b = A_b T^{B_b} e^{-\frac{C_b}{T}}$$

The values of the forward and backward constants  $A, B$  and  $C$  are obtained from the modified Dunn - Kang chemical kinetics model <sup>3</sup>.

The species mass fraction can then be obtained from the chemical concentration using this relation

$$\rho c_i = [X_i] M_i$$

### Thermodynamics

Since the gas is not calorically perfect, we can no longer assume that the internal energy is proportional to the temperature, but rather, we must take into account the vibrational and zero point energies as well. Assuming that the gas does not ionize



and is in vibrational equilibrium, the internal energy of *each individual specie* of the gas is

$$e_i = \frac{\frac{5}{2}R_u T + R_u \frac{\theta_i}{\left(e^{\frac{\theta_i}{T}} - 1\right)} + (\Delta H_f)_i^0}{M_i} \text{ for molecules}$$

$$e_i = \frac{\frac{3}{2}R_u T + (\Delta H_f)_i^0}{M_i} \text{ for atoms}$$

where the energy of the gas *mixture* is

$$e = \sum_i e_i c_i$$

and the gas constant is

$$R = R_u \sum_i \left( \frac{c_i}{M_i} \right)$$

The change in the standard heat of formation,  $(\Delta H_f)_i^0$ , is the "effective" change of the zero point energies between the products and the reactants of species *i*.

Therefore, in order to obtain the temperature, an iterative procedure must be used. In this study, a two step linear extrapolation, was used to calculate the temperature based on the local internal energy of the gas mixture, where the internal energy is a function solely of the temperature and the chemical composition. Since the internal energy is *dominantly* linear, that is the effect of the non-linearity due to the vibrational energy terms is small, the usage of a linear extrapolation is justified. It has been found that that this method was easy to code, accurate, and very efficient.

## Transport properties

The transport coefficients  $\mu$  and  $k$  are no longer simple functions of temperature. For a chemically reacting gas, they must be determined for each specie and then combined to calculate the value for the gas mixture. This also applies to the chemical diffusivity  $\mathcal{D}$ .

For the individual species, the viscosity and thermal conduction coefficients are

$$\mu_i = 2.6693 \times 10^{-5} \frac{\sqrt{M_i T}}{d^2 \Omega_\mu}$$

$$k_i = 8.3221 \times 10^{-2} \frac{\sqrt{\frac{T}{M_i}}}{d^2 \Omega_k}$$

where  $d$  is a characteristic molecular diameter, and the collision integrals are a function of temperature and the Leonard Jones parameters

$$\Omega_\mu = \Omega_k = f\left(\frac{T}{\varepsilon/k_1}\right)$$

The diffusivity for a binary system (i.e a two component system) can be calculated in a similar fashion

$$D_{ij} = 0.0188297 \frac{\sqrt{T^3 \left(\frac{1}{M_i} + \frac{1}{M_j}\right)}}{p d_{ij}^2 \Omega_{d,ij}}$$

where

$$d_{ij} = \frac{1}{2} (d_i + d_j) \text{ average diameter}$$

$$\Omega_{d,ij} = f\left(\frac{T}{\varepsilon_{ij}/k_1}\right)$$

$$\frac{\varepsilon_{ij}}{k_1} = \sqrt{\frac{\varepsilon_i}{k_1} \frac{\varepsilon_j}{k_1}}$$

The transport properties for the gas mixture can then be evaluated from the individual components. For  $\mu$  and  $k$ , Wilkes mixture rule is applicable. To calculate the multi component diffusivity,  $D_{im}$ , the following approximation was used

$$D_{im} = \frac{1 - X_i}{\sum_j \frac{X_j}{D_{ij}}}$$

Fick's Law for a multi-component gas is

$$J_i = \text{mass flux of species } i = -\rho D_{im} \nabla c_i$$

## 2.3 Numerical Method

The flowfield has been solved with MacCormack's explicit predictor-corrector technique, a time dependent method which solves the combined hyperbolic-elliptic equations that are characteristic of the supersonic and subsonic flow regimes that occur in supersonic viscous flow problems.

The flowfield is solved on a two-dimensional rectangular grid which includes the plate surface and the freestream.

MacCormack's technique solves the first order Taylor series representation by using a predictor-corrector scheme to obtain second order accuracy. MacCormack's predictor-corrector technique is explained in reference .

### 3 Preliminary Results

In this section, preliminary results are given that illustrate the effects of wall catalycity on a shock wave / boundary layer interaction. To do this, separate numerical solutions are shown for the calorically perfect case, chemically reacting non-catalytic case and the chemically reacting fully-catalytic case. Then a direct comparison of the surface heat transfer and shear stress between the three cases is made.

For each of the three cases, the following parameters were constant.

Table 1 Freestream parameters

$M_{inf}$	5.0
incident shock angle	30 deg
$T_{wall}$	1087 K
$T_{inf}$	1087 K
Re	1793
$\rho_{inf}$	3.194 E-4 kg/m <sup>3</sup>
$c_p$	1.48
R	413.55 J/kg
grid size	70 x 80
plate length	0.06 m

For the chemically reacting cases the following inflow species mass fractions were used.

Table 2 Inlet species mass fractions for chemically reacting cases

Specie	Mass fraction
O <sub>2</sub>	1.458 E-5
O	2.388 E-1
N <sub>2</sub>	5.500 E-1
N	2.111 E-1
NO	3.389 E-3

These conditions correspond to chemically frozen flow that has isentropically expanded around the blunt forebody of a hypersonic vehicle travelling at Mach 25 at an altitude of 60 Km.

### 3.1 Calorically Perfect Gas

The first step towards modeling a shock / boundary layer interaction with nonequilibrium chemistry and a fully catalytic wall, is to investigate the *fluid dynamic* effects of the interaction. This is done by neglecting the nonequilibrium chemical effects, thus assuming that the gas is calorically perfect.

Figure 3 is a pressure contour of the calorically perfect flowfield. The large pressure gradients clearly emphasize the incident shock, the shock emanating from the leading edge as well as the shock in front of the separation zone. Also, the expansion fan on the backside of the separation zone and the compression waves that begin to coalesce into the reflected shock are apparent. Because the local flow velocity is very small, the pressure remains fairly constant inside the separation zone.

Figure 4 is a temperature contour of calorically perfect flowfield. Again, the incident shock as well as the shocks emanating from the from the leading edge and the front of the separation zone are easily recognizable. The maximum temperature occurs behind the reattachment compression waves. Because the surface is assumed to be a cold wall, the maximum temperature occurs not *at* the surface, but rather a

small distance *above* the surface. Also, the temperature gradient at the wall is much smaller inside the separation region, than the gradient outside the separation region.

A Mach contour of the flowfield is shown in figure 5. The bold line represents the sonic line. We can see that a large amount of the flow is subsonic, especially around the separation region. But of greater concern, there is a significant subsonic region at the outflow. This region has the *potential* of causing numerical difficulties, especially if the reversed flow inside the separation region becomes too close to the outflow plane. If this was to happen, the outflow plane may experience reversed flow that would 'feed' mass into the separation zone, thus expanding it indefinitely until the entire computational domain is engulfed by the separation zone. This is obviously *not* physically accurate. So care must be taken when prescribing the plate length so that there is sufficient space between the back of the separation zone and the outflow plane.

The direction and magnitude of the velocities inside the flowfield is illustrated in a velocity vector plot, as seen in figure 6. The velocity vector plot emphasizes the reversed flow inside the separation region. Though not as visually apparent, the various shocks that occur in the flowfield, as well as the boundary layers before and after the separation region can also be seen.

A major concern when executing a time marching codes is when is a converged solution achieved. In response to this dilemma, the heat transfer along the surface of the plate has been plotted in figure 7 for various time steps ranging from 6000 to 40,000 (for flat plate boundary layer flows, 2000 time steps were sufficient for convergence). The heat transfer data in this figure was calculated using a coarser grid (40 x 50 ) in order to emphasize the problem with convergence. Because the surface heat transfer is the focus of this paper, the surface heat transfer was chosen to be 'yardstick' to determine whether the solution is properly converged with respect to time.

We can see from figure 7 that as time progresses, the surface heat transfer is slowly decreasing in front of and behind the separation region. This is because the separation

region is continuously expanding. Even after 40,000 time steps the solution hasn't *fully* converged. This result supports the possibility that the shock wave / boundary layer interaction may not be a completely steady problem. But, the *magnitude* of change between time steps becomes *very small* and the calorically perfect flow may be *considered* to be converged at 20,000 time steps. However, when coupled with a fully catalytic wall which is a source of a large amount of energy transfer, the growth of the separated region may not be so mild, and the question of when a converged solution is obtained may be more difficult to answer. This problem will be discussed later.

### 3.2 Chemically Reacting Gas / Non-Catalytic Wall

For the chemically reacting / non-catalytic wall case, results are given that determine whether non-equilibrium chemistry plays a significant role in the shock wave / boundary layer interaction.

Figures 8, 9 and 10 are the pressure contour, temperature contour and velocity vector plot respectively for the chemically reacting flowfield. We can see that both qualitatively and quantitatively, that there is little difference between the chemically reacting and calorically perfect results.

Figures 11 thru 15 are contour plots of each of the species mass fractions. The plots for monatomic oxygen and monatomic nitrogen best illustrate that most of the chemical recombination occurs immediately *upstream* of the separation region. For nitrogen, there is a slight amount of *dissociation* inside the separation region. This dissociation could actually *lower* the peak heat transfer that occurs behind the reattachment point. The magnitudes, however, of the dissociation and recombination for both oxygen and nitrogen are quite small. The percent differences between the maximum and minimum mass fractions inside the flowfield for monatomic oxygen and nitrogen are 0.70% and 0.95% respectively. Therefore, we can consider the flow to be essentially *chemically frozen*.

It is important to emphasize that both the qualitative and quantitative results are dependent upon flow conditions; wall and freestream temperatures, Reynolds numbers and especially inlet species mass fractions. Therefore any conclusions that can be drawn from these results may not be applicable for all flow scenarios.

### 3.3 Chemically Reacting Gas / Fully-Catalytic Wall

In this section results are given for the chemically reacting fully catalytic wall case. These results will illustrate the effects of surface catalycity on the separated flow.

Figures 16, 17 and 18 are the respective pressure contour, temperature contour and velocity vector plot for this case. Figures 19 thru 23 are the contour plots for the distribution of each of the mass fractions throughout the flowfield. The most apparent feature of these results is that the catalytic surface *dominates* the species mass fraction gradients. Although it appears graphically that chemical reactions do not occur in the rest of the flowfield away from the wall, this is not true.

A main concern of this paper is the coupled interaction between the separation zone and the catalytic surface. Let us discuss the effects of the *separation zone on the catalytic surface*. From the contour plots of O and especially N, we can see that the mass fraction gradient inside the separation zone is relatively mild. In the case of the monatomic nitrogen mass fraction, the large gradients encircle the separation zone so that the dramatic effects of the catalytic wall is 'pushed' away from the surface in the separation region. The largest gradients of the species mass fractions occur behind the reattachment point, which further increases the heat transfer at the location where the maximum heat transfer is expected to occur.

The production of nitric oxide, NO, has become significant inside the separation zone for the fully catalytic wall case. This is important because though the production of NO from the atomic species in the freestream is exothermic, it is considerably less exothermic than the production of diatomic nitrogen and oxygen. Therefore the

surface heat transfer in the separation zone is reduced due to the inclusion of nitric oxide in the chemistry modeling.

There are also direct effects of *the catalytic surface on the separation zone*. Because of all the energy transfer due to chemical recombination, especially on the fringes of the separation zone, the separation zone increases in size. This, in turn, increases the strength of the shock immediately upstream of the separation zone, thus slowing the flow further and allowing it more time for chemical recombination. This coupling effect makes it very difficult to obtain results that converge properly with respect to time. It was required to considerably increase the grid density to accommodate the large gradients at the wall and to 'numerically distinguish' between the front of the separation zone and the leading edge. In other words, there must be enough grid points placed in the front end of the plate surface so that the large gradients that occur at the leading edge (which are admittedly inaccurate) do not affect the the front of the separation zone and cause large numerical errors. It was found that the inclusion of a sufficiently dense grid allowed a steady state solution to be obtained (i.e. a solution that has converged with time).

### 3.4 Comparisons of Results

A Direct Comparison of the wall heat transfer between all three cases is shown in figure 24. Compared to the calorically perfect case, we can see that there is a small decrease in the heat transfer for the non-catalytic wall case. The change in the maximum heat transfer (not including the leading edge of the plate) is only 5.8%. Though this value may be significant when a very accurate estimate of the surface heat transfer is required, it is essentially negligible for most preliminary design purposes. Again, it should be noted that the difference in the heat transfer is *very* dependent upon the values used for the inlet species mass fractions.

However, when we include the effects of wall catalycity, there is a *monstrous* increase of 141% for the surface heat transfer, as compared to the calorically perfect



case. This was to be expected, considering the amount of energy that is being released at the surface due to *instantaneous* chemical recombination.

A similar comparison is made for the surface skin friction, as shown in figure 25. One purpose of the skin friction plot is to effectively illustrate the size of the separation zone. The region where the skin friction is negative (below the dotted line) the flow is reversed. We can see from this figure that the nonequilibrium chemistry in the non-catalytic wall case significantly increases the size of the separation zone. Also, the separation zone is further expanded in the fully-catalytic wall case. Although the effects of wall catalycity on the surface skin friction is not nearly as dramatic as the effects on the surface heat transfer.

## 4 Conclusions

The following conclusions can be made from this study concerning the effects on the shock wave / boundary layer interaction

1. Wall catalycity *significantly* increased the surface heat transfer and must be accounted for when designing a hypersonic vehicle.
2. The effects of nonequilibrium chemistry, as demonstrated in the non-catalytic wall case, is very small. Therefore the flow is essentially *chemically frozen*.

## 5 Further Research

Though presently the study is essentially complete, there are still a few areas that will require further investigation.

1. **Grid convergence.** Among the largest problems in CFD is code validation. Though this code was successfully validated for the calorically perfect case, validation is still required for the chemically reacting cases, especially for the fully-catalytic wall. A very effective means of validation is grid convergence, where identical results can be produced on a denser grid.
2. **Higher Reynolds number flow.** In order to better predict realistic flowfields, a larger Reynolds number case must be run. Because of practical computer restrictions, this will require a condensed grid. That is, a non-uniform grid whose spacings are smaller near the wall and the leading edge of the plate.

These additions will hopefully be included at the time of the presentation of this paper.

## References

1. Delery, J "Shock / Shock and Shock Wave / Boundary Layer Interactions in Hypersonic Flows" *AGARD-FDP-VKI Special Course on Aerothermodynamics of Hypersonic Vehicles* Onera — 92320 Chatillon, France, June 1988
2. Dryden Research Lectureship, AIAA 28th Aerospace Sciences Meeting, Reno, 1990
3. Erickson, R. W. "The Non-Equilibrium Chemistry Behind a Mach 25 Normal Shock (2nd Edition)" University of Maryland, 1989
4. Anderson, J. D. Jr. *Hypersonic and High Temperature Gas Dynamics* McGraw Hill, 1989
5. Taylor, H. S. *Combustion Processes* Vol II of the High Speed Aerodynamics and Jet Propulsion Series, Edited by Lewis, B. Princeton University Press, 1956
6. Reid, R. C. Praunitz, B. E Poling, *The Properties of Gases and Liquids (4th Edition)* McGraw Hill, 1987
7. Svehla, R. A. "Estimate Viscosities and Thermal Conductivities of Gases at High Temperatures" National Aeronautics and Space Administration, Technical Report R-132, 1962
8. Van Driest, E. R. "Investigations of Laminar Boundary Layer in Compressible Fluids Using the Crocco Method" National Advisory Committee for Aeronautics, TN 2597, 1952
9. Hirshfelder, J. O. Curtis, C. F. Bird, R. B. *Molecular Theory of Gases and Liquids*

John Wiley & Sons, 1954

10. Bird, R. B. Stewart, W. E. Lightfoot, E. N. *Transport Phenomena* John Wiley & Sons, 1960

# Figures of Results

Calorically Perfect Gas

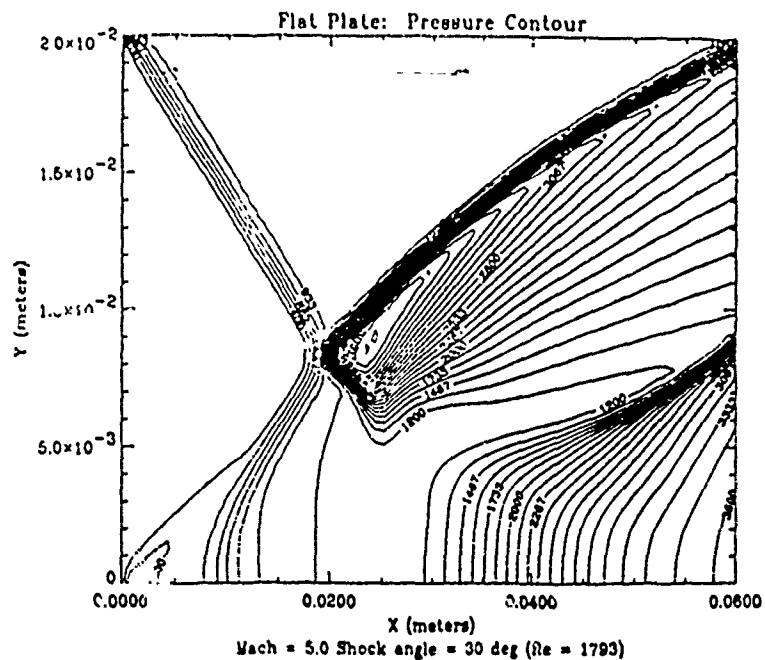


Figure 3 Pressure Contour Plot

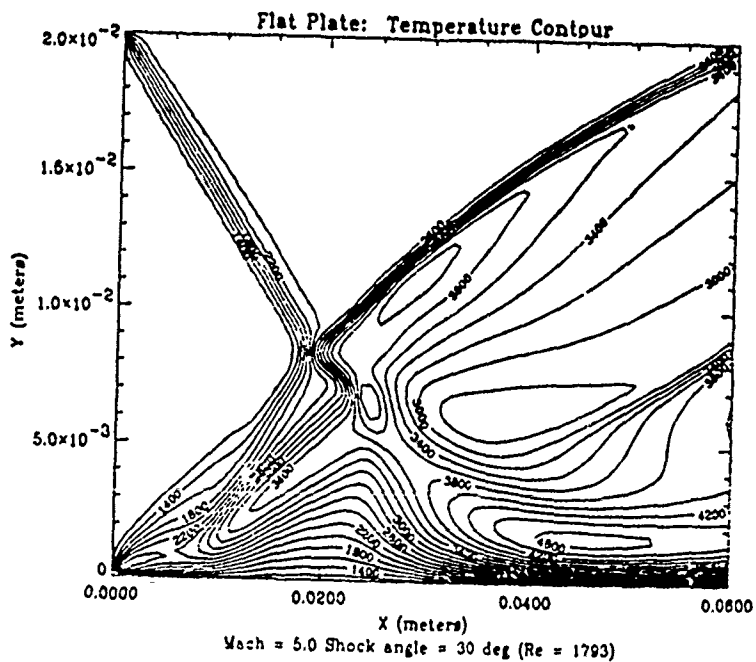


Figure 4 Temperature Contour Plot

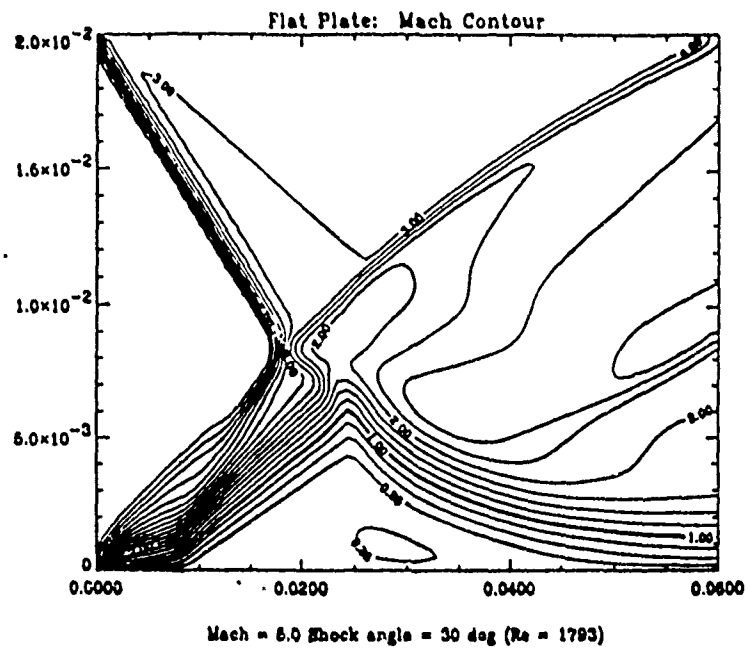


Figure 5 Mach Number Contour Plot

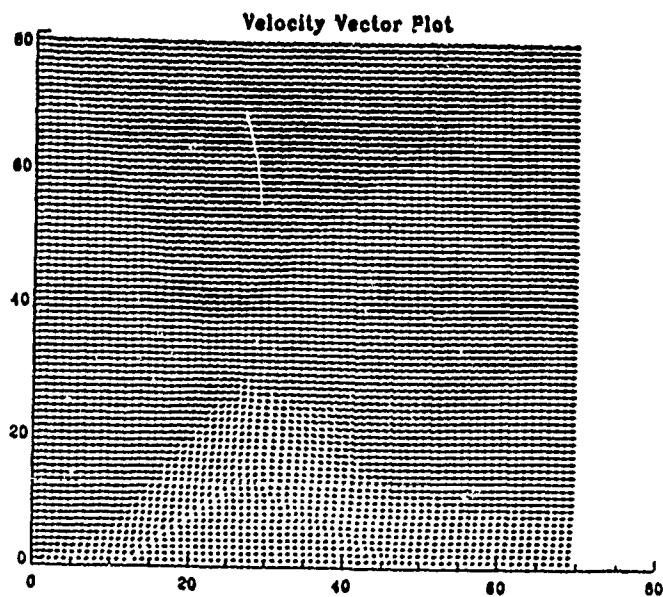


Figure 6 Velocity Vector Plot

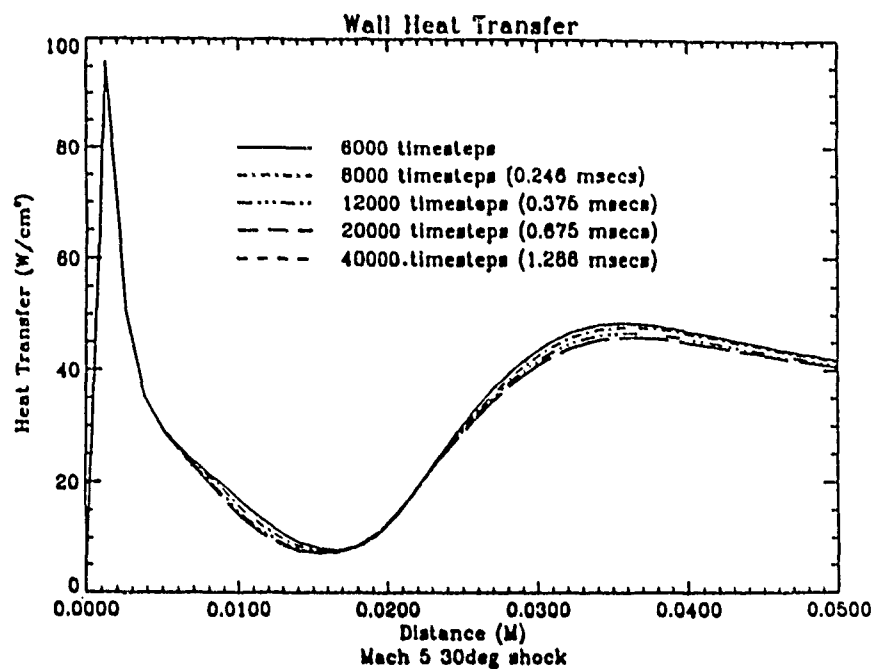


Figure 7 Plot of Transient Surface Heat Transfer

# Non-Catalytic Wall

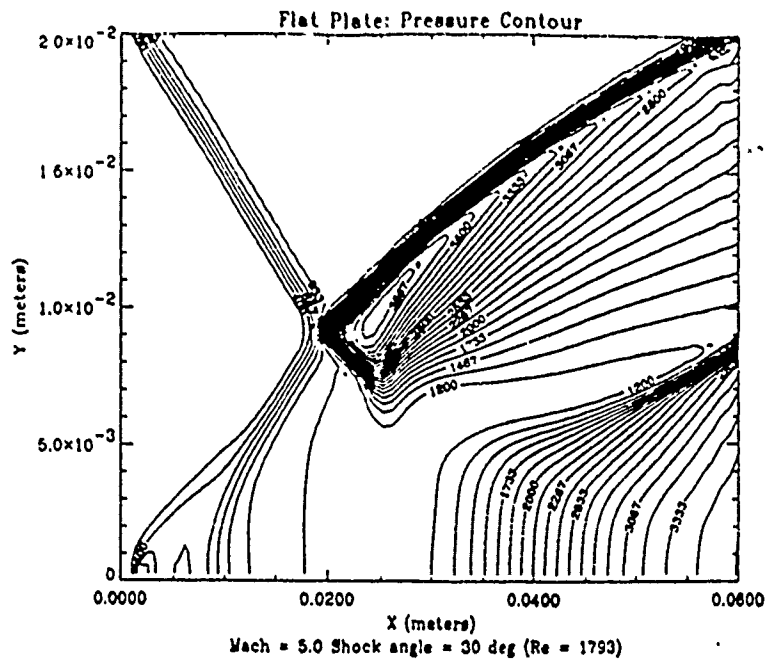


Figure 8 Pressure Contour Plot

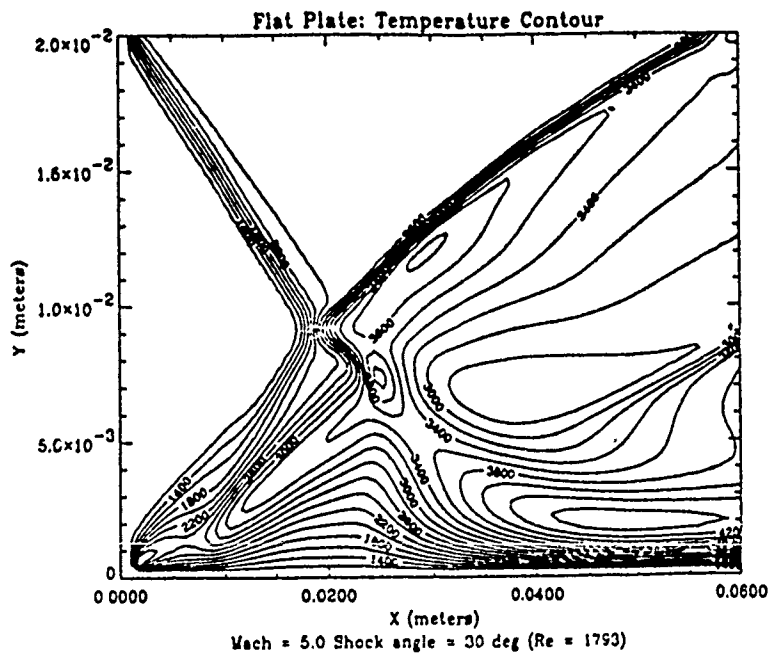


Figure 9 Temperature Contour Plot



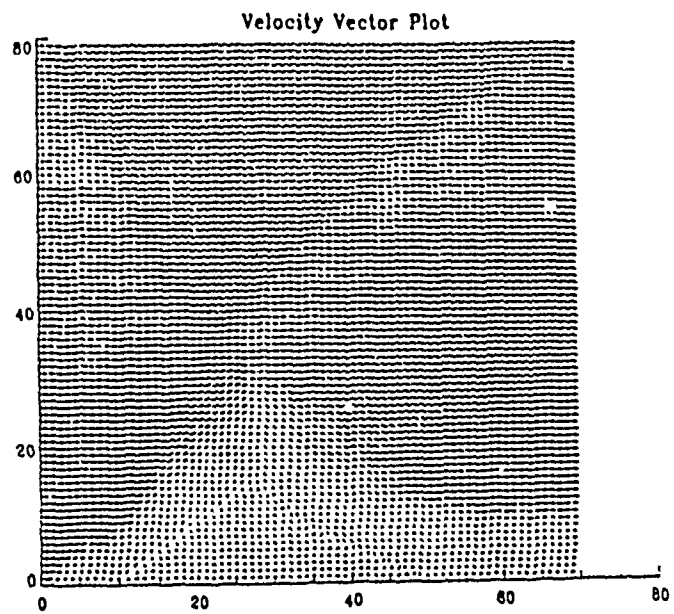


Figure 10 Velocity Vector Plot

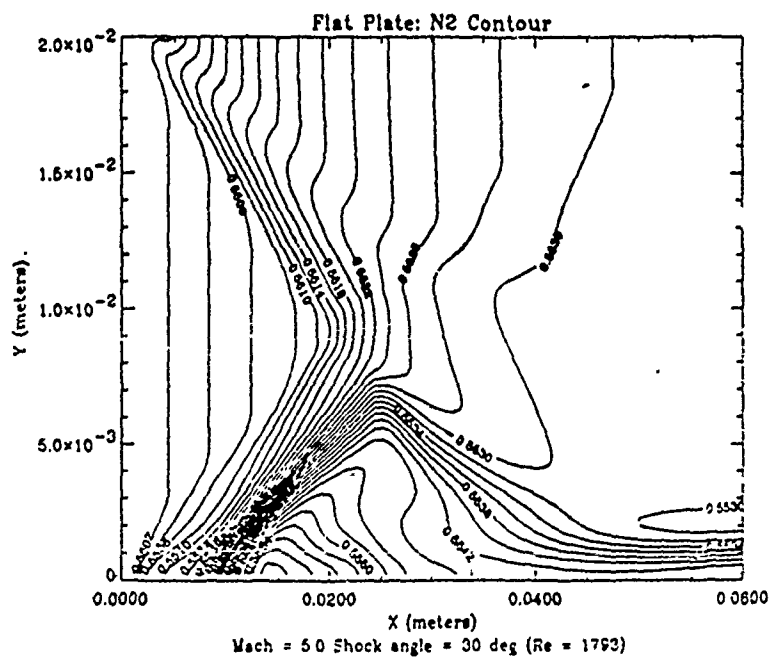


Figure 11 N<sub>2</sub> Contour Plot

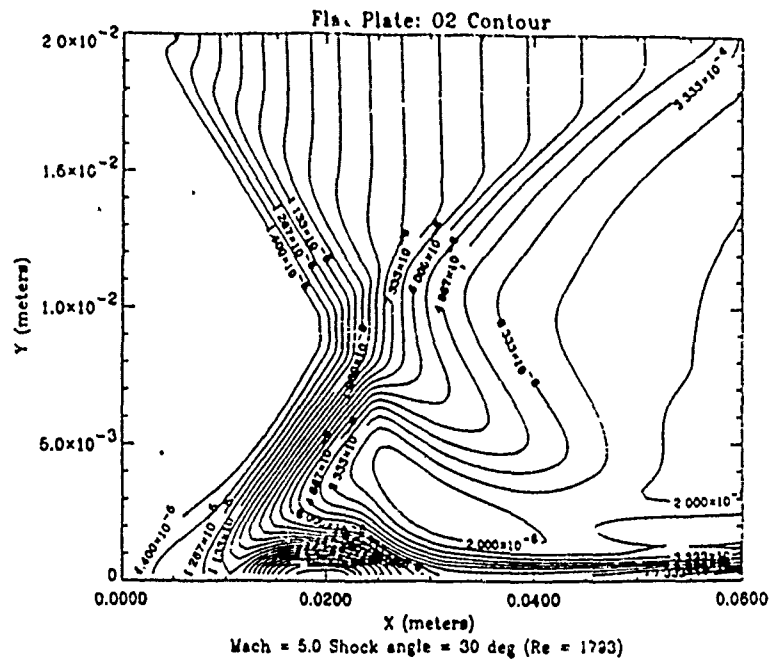


Figure 12 O2 Contour Plot

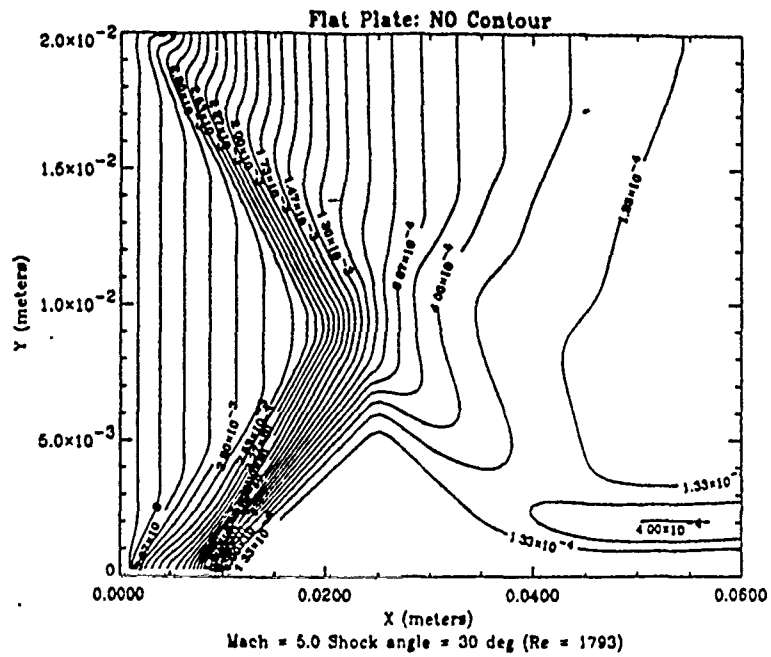


Figure 13 NO Contour Plot



# Fully-Catalytic Wall

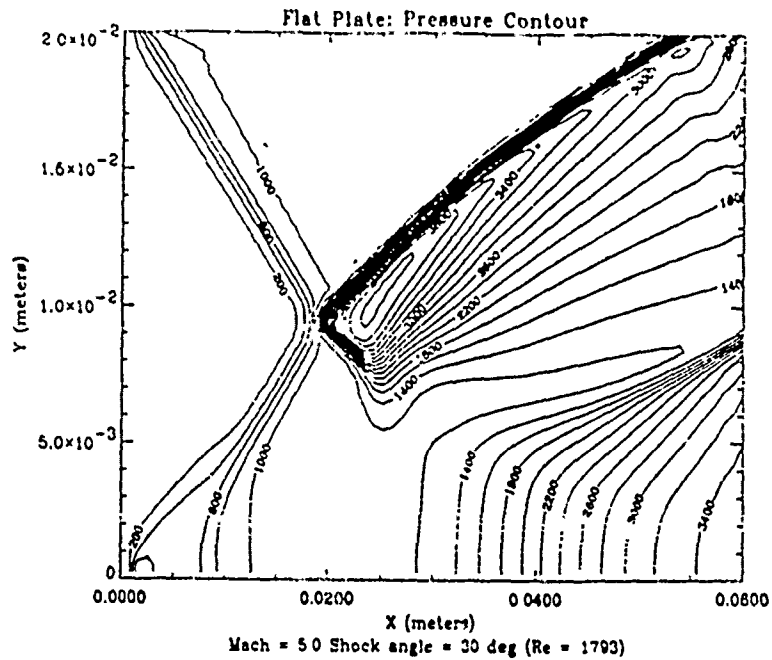


Figure 16 Pressure Contour Plot

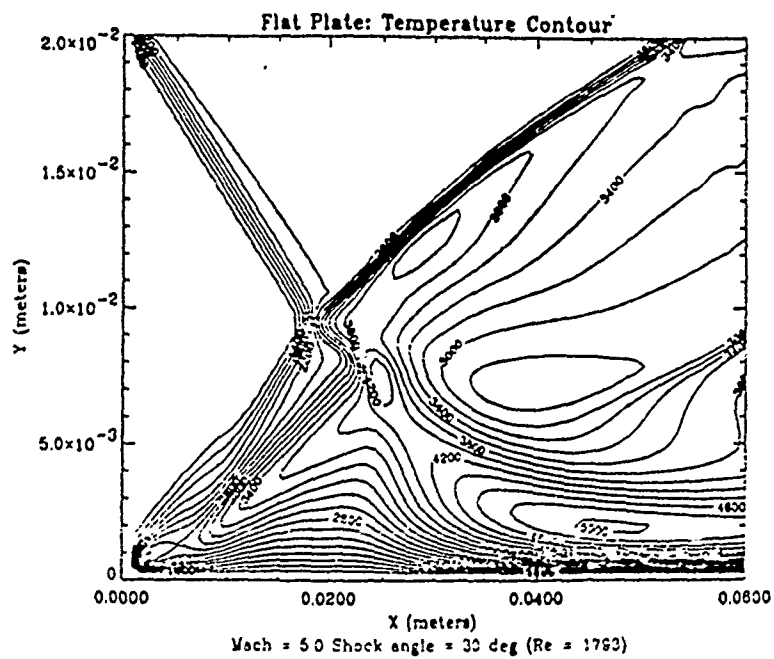


Figure 17 Temperature Contour Plot

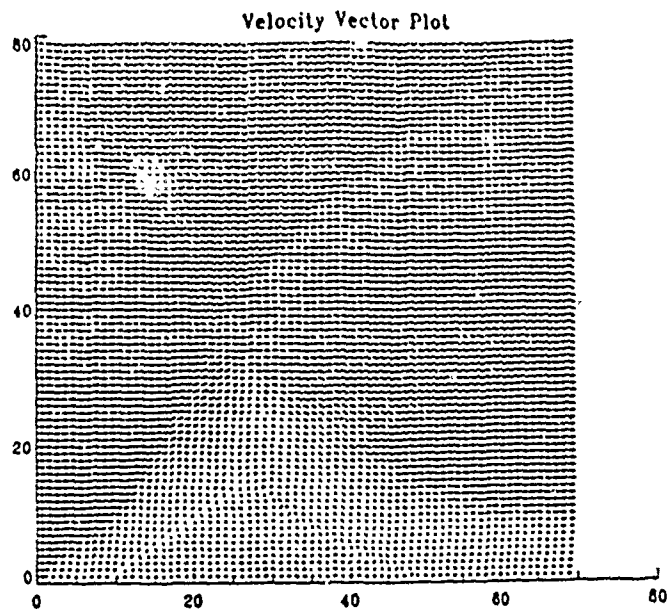


Figure 18 Velocity Vector Plot

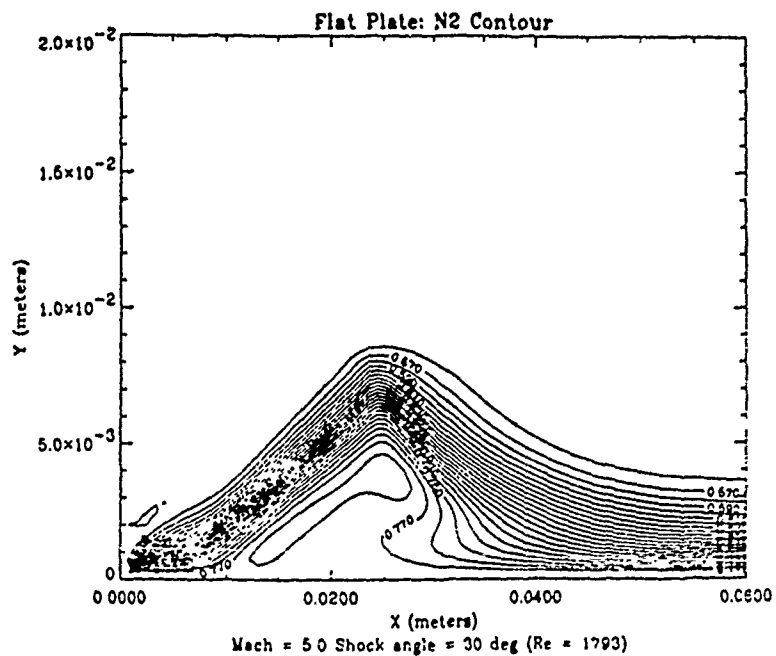


Figure 19 N2 Contour Plot

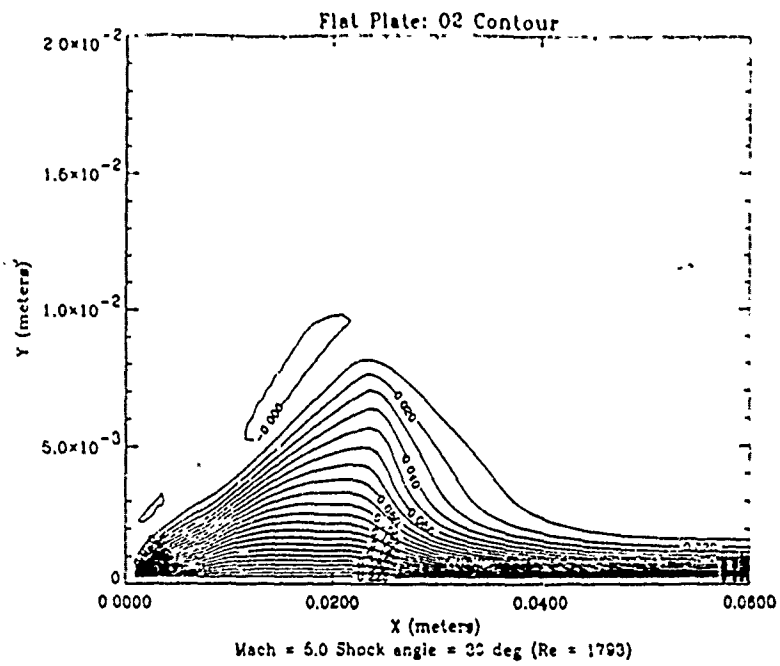


Figure 20 O2 Contour Plot

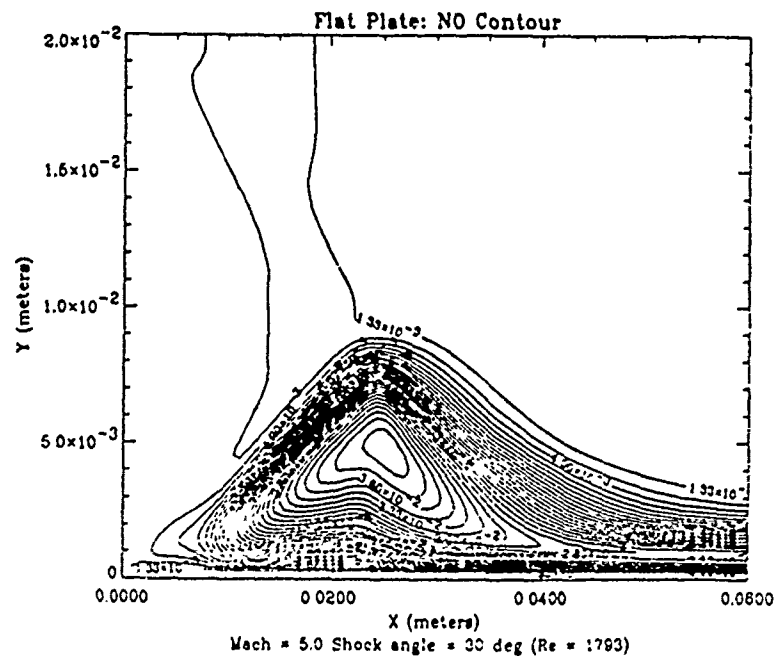


Figure 21 NO Contour Plot

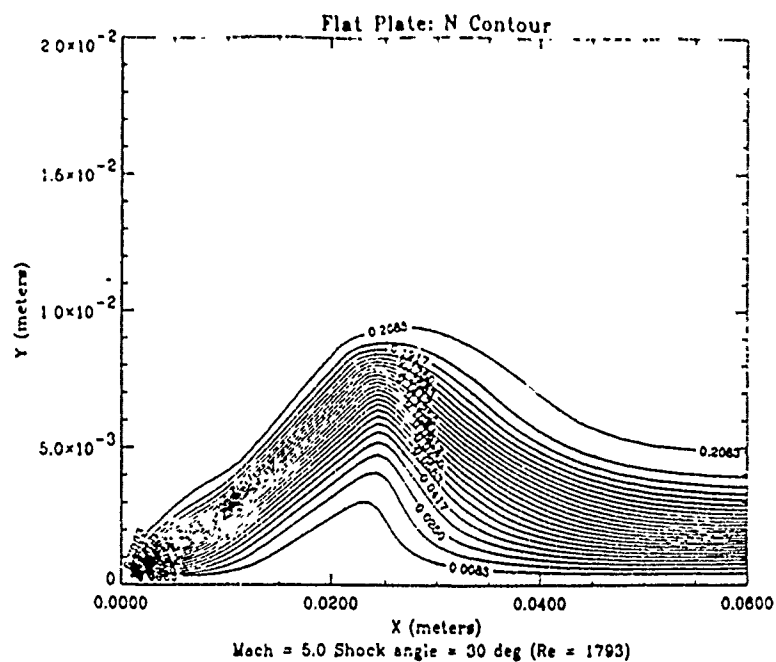


Figure 22 N Contour Plot

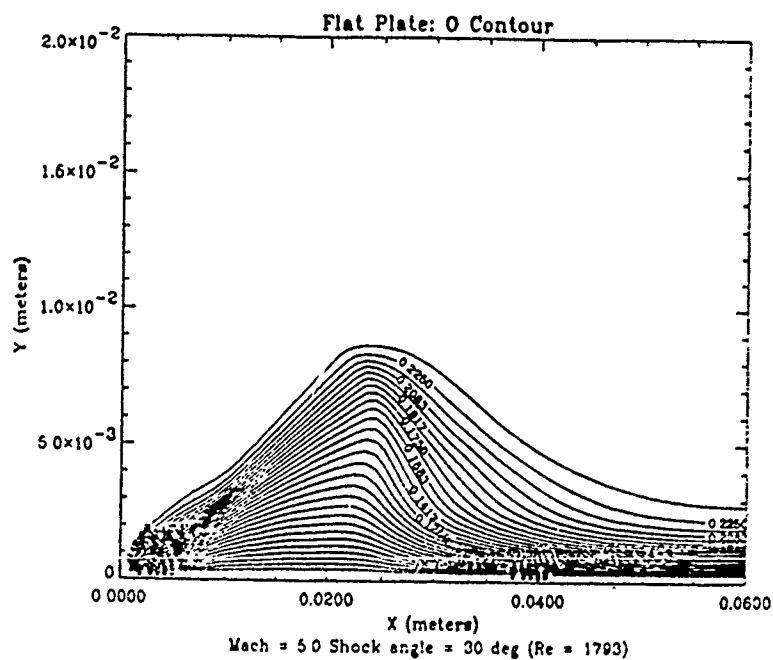


Figure 23 O Contour Plot

## Comparative Results

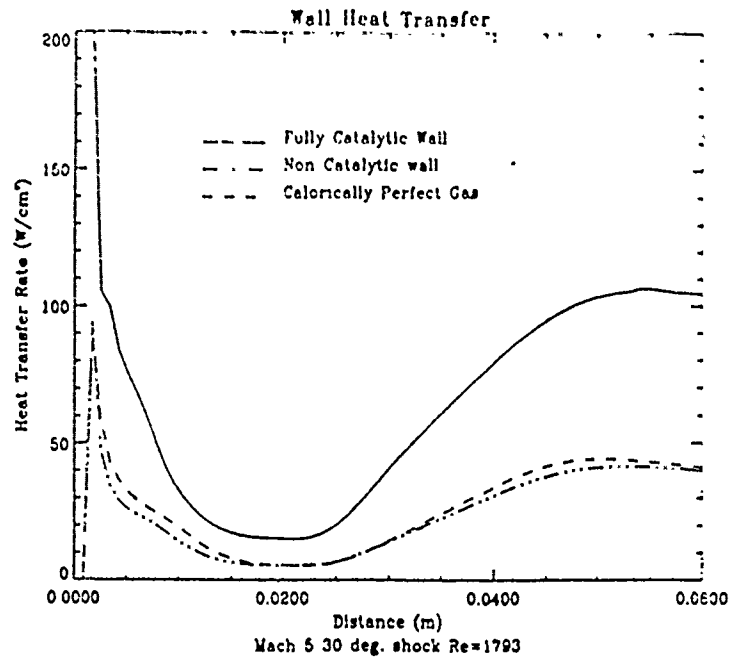


Figure 24 Surface Heat Transfer

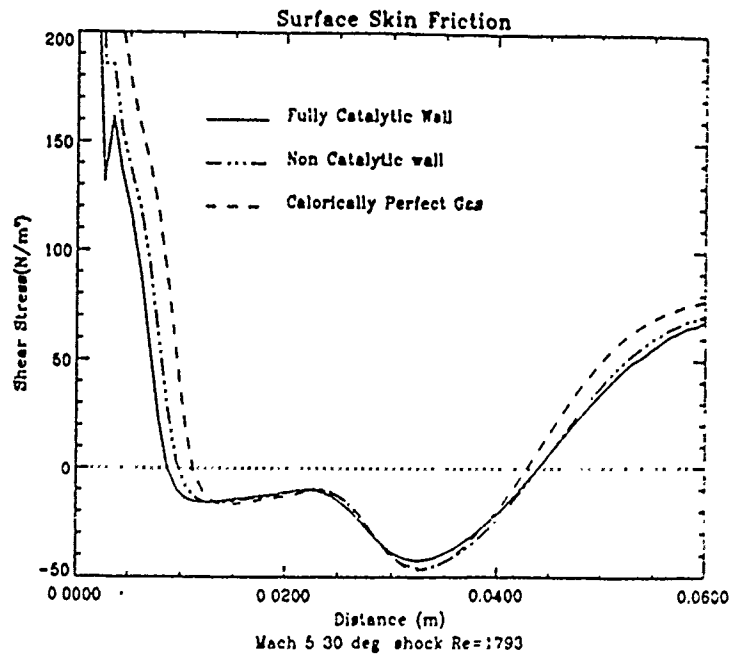


Figure 25 Surface Skin Friction